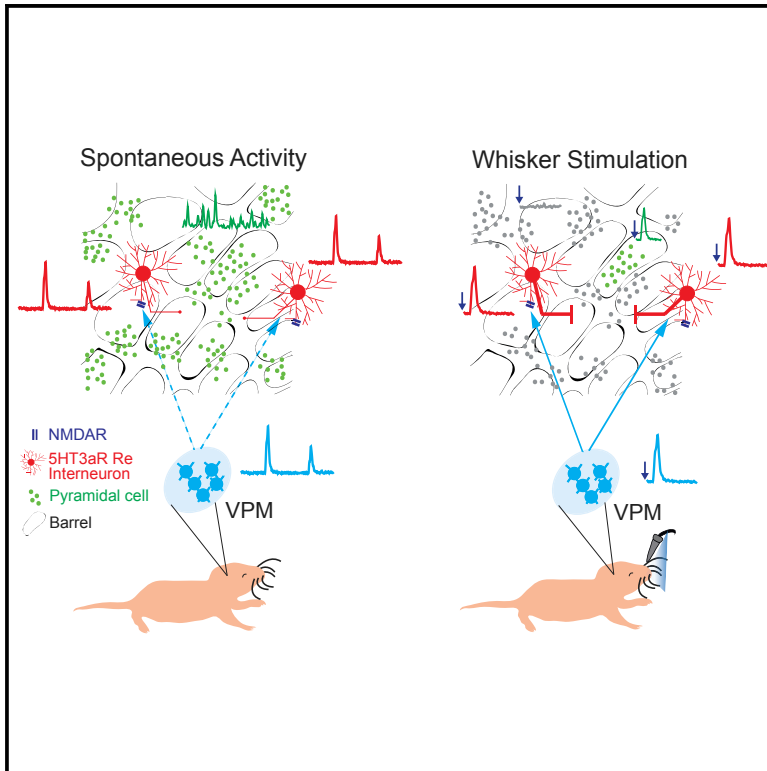


Layer I Interneurons Sharpen Sensory Maps during Neonatal Development

Graphical Abstract



Authors

Alicia Che, Rachel Babij,
Andrew F. Iannone, ..., Conor Liston,
Gord Fishell,
Natalia V. De Marco García

Correspondence

nad2018@med.cornell.edu

In Brief

Che et al. combine genetic tools and longitudinal *in vivo* calcium imaging in young mouse pups to show that superficial interneurons participate in a transient thalamocortical circuit. Their recruitment is critical for the emergence of sensory maps and sensory discrimination.

Highlights

- 5HT3aR Re interneurons in LI barrel cortex desynchronize by the second postnatal week
- Whisker stimulation recruits 5HT3aR Re interneurons in the first postnatal week
- Sensory deprivation and NMDAR knockdown in 5HT3aR Re interneurons disrupt synchrony
- 5HT3aR Re interneurons constrain pyramidal cell activation and barrel size



Layer I Interneurons Sharpen Sensory Maps during Neonatal Development

Alicia Che,¹ Rachel Babij,^{1,2} Andrew F. Iannone,^{1,2} Robert N. Fetcho,^{1,2} Monica Ferrer,^{1,4} Conor Liston,¹ Gord Fishell,³ and Natalia V. De Marco García^{1,5,*}

¹Center for Neurogenetics, Brain and Mind Research Institute, Weill Cornell Medical College, New York, NY 10021, USA

²Weill Cornell/Rockefeller/Sloan Kettering Tri-Institutional MD-PhD Program, New York, NY 10021, USA

³Harvard Medical School and the Stanley Center at the Broad, Cambridge, MA 02142, USA

⁴Present address: Yale School of Medicine, New Haven, CT 06510, USA

⁵Lead Contact

*Correspondence: nad2018@med.cornell.edu

<https://doi.org/10.1016/j.neuron.2018.06.002>

SUMMARY

The neonatal mammal faces an array of sensory stimuli when diverse neuronal types have yet to form sensory maps. How these inputs interact with intrinsic neuronal activity to facilitate circuit assembly is not well understood. By using longitudinal calcium imaging in unanesthetized mouse pups, we show that layer I (LI) interneurons, delineated by co-expression of the 5HT3a serotonin receptor (5HT3aR) and reelin (Re), display spontaneous calcium transients with the highest degree of synchrony among cell types present in the superficial barrel cortex at postnatal day 6 (P6). 5HT3aR Re interneurons are activated by whisker stimulation during this period, and sensory deprivation induces decorrelation of their activity. Moreover, attenuation of thalamic inputs through knockdown of NMDA receptors (NMDARs) in these interneurons results in expansion of whisker responses, aberrant barrel map formation, and deficits in whisker-dependent behavior. These results indicate that recruitment of specific interneuron types during development is critical for adult somatosensory function.

INTRODUCTION

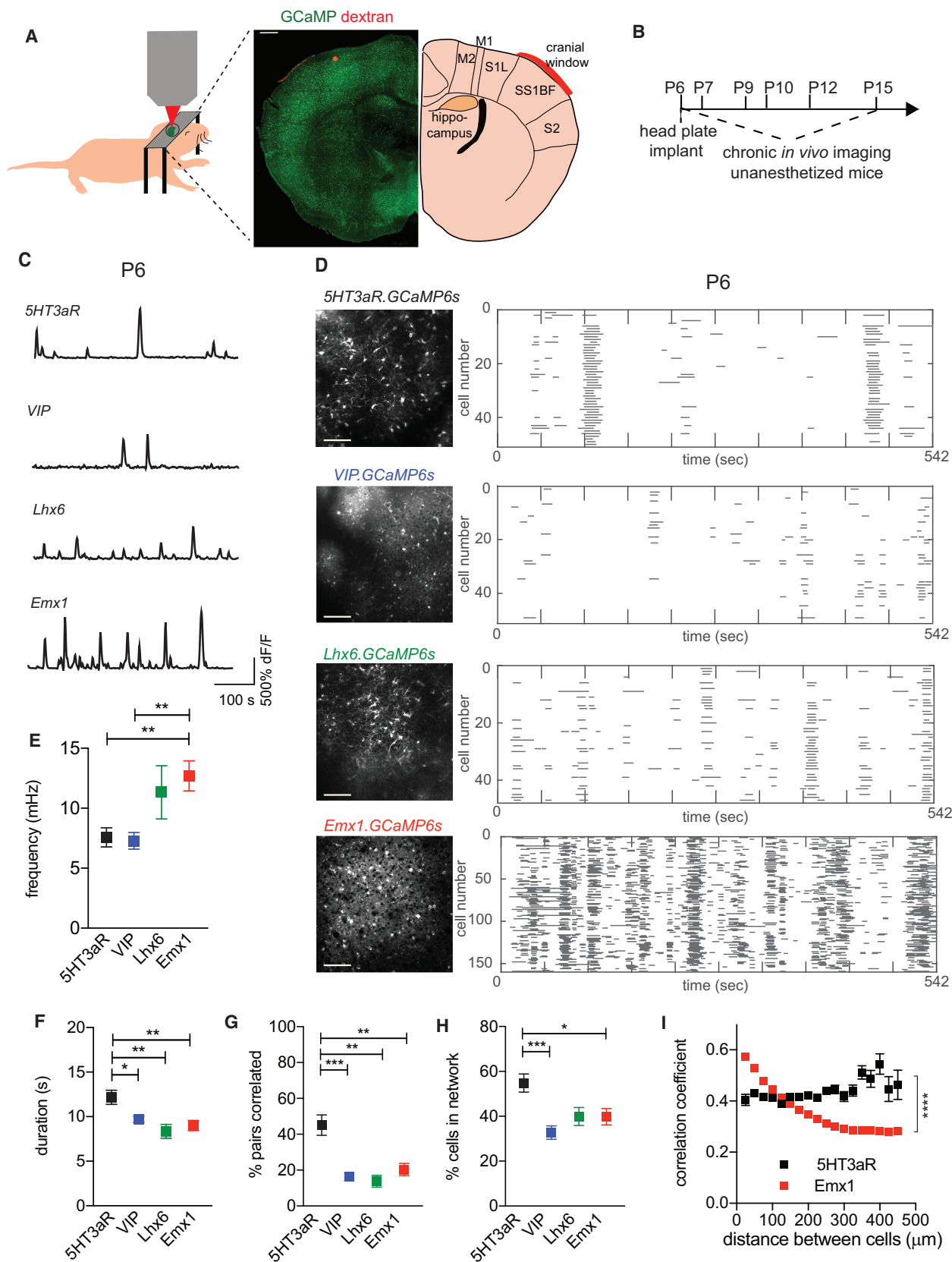
Early neuronal networks are dominated by synchronous activity that shapes the maturation of circuits at perinatal stages (Kirkby et al., 2013; Leighton and Lohmann, 2016). Although different patterns of activity have been identified in sensory areas, it is unclear how early experience interacts with intrinsic programs to shape the topographic representations of the external world in the brain.

Electrical recordings and imaging of neuronal populations indicate that the emergence of topographic maps cannot be solely explained by a spatial confinement of spontaneous activity. While intrinsically generated events can coexist with those triggered by sensory experience (Burbridge et al., 2014; Chiu and Weliky, 2001; Shen and Colonnese, 2016; Siegel et al.,

2012), these two types of synchronous events often reflect the activation of different neuronal ensembles. In the barrel cortex, a region of the somatosensory cortex that contains a topographic representation of the whiskers (barrels) (Petersen, 2007; Woolsey and Van der Loos, 1970), sensory inputs can trigger barrel-specific activity from birth. These inputs consist of passive whisker deflections, as well as sensory feedback from spontaneous myoclonic twitches, and are present before the onset of active whisking by the end of the second postnatal week (Akhmetshina et al., 2016; Khazipov et al., 2004; Yang et al., 2013). In contrast, intrinsically driven activity, which is also prominent at these stages, can follow non-barrel-specific patterns (Allène et al., 2008; Golshani et al., 2009; Yuste et al., 1992). Thus, the somatosensory system provides an ideal model to study how different activity-dependent programs are selectively recruited to allow for the emergence of functional topography.

Pharmacological evidence suggests that network activity during the first postnatal week is likely coordinated by excitatory and inhibitory neurons. Synchronous activity is predominately mediated by excitatory transmission in the barrel cortex of newborn pups, whereas inhibition regulates rhythmic activity by the end of the first postnatal week (Minlebaev et al., 2007, 2011). Despite its prominence, it is unclear how synchronous activity maps onto genetically defined developing interneurons. In this study, we assessed the intrinsic and sensory-driven responses of interneurons and excitatory cells *in vivo* using the genetically encoded calcium sensor GCaMP6s (Chen et al., 2013) and determined how perturbation in these responses affects the development of topographic maps from the first to the second postnatal week. We show that the 5HT3aR Re interneurons display slow calcium transients with significantly higher duration and correlation compared to those observed in other populations at postnatal day 6 (P6). These transients become decorrelated in the second postnatal week alongside a prominent reduction in direct thalamic inputs. We present evidence that whisker stimulation evokes responses in 5HT3aR Re interneurons as early as P6. Furthermore, sensory deprivation from birth causes a significant reduction in the correlation of interneuron—but not excitatory neuron—activity at P6. Similarly, disrupting thalamic inputs onto 5HT3aR Re interneurons by genetically ablating NMDA receptors (NMDARs) leads to a decrease in synchrony at the same





(legend on next page)

stage. 5HT3aR Re dysfunction results in the broadening of cortical responses to whisker stimulation, a structural enlargement of barrels, and in adult animals, impaired texture discrimination.

Based on these results, we propose that 5HT3aR Re interneurons coordinate the formation of topographic maps by suppressing ongoing spontaneous activity in superficial networks in response to sensory stimulation. The dependence on sensory experience for the proper function of inhibitory networks at neonatal stages sharply contrasts with previously described evidence of sensory-independent emergence of excitatory networks. Our results indicate that the interaction of both inhibitory and excitatory activity patterns is fundamental for cortical circuit assembly during the first postnatal week.

RESULTS

Cell-type-Specific Patterns of Neuronal Activity in Neonatal Mice

To achieve selective GCaMP6s expression in developing interneurons and excitatory neurons, we crossed cell-type-specific Cre driver lines to *RCL-GCaMP6s* mice (Ai96) (Figure 1; also see STAR Methods). Cortical interneurons arise almost entirely from the medial and caudal ganglionic eminences (MGE and CGE, respectively) (Batista-Brito and Fishell, 2009). CGE interneurons, delineated by 5HT3aR expression, are the most abundant population in supra-granular layers of the cortex and co-express either Re or vasoactive intestinal peptide (VIP) (Lee et al., 2010). In contrast, MGE-derived interneurons are delineated by LIM homeobox 6 (*Lhx6*) expression at early stages of development (Marin et al., 2000). We recorded chronically the same genetically defined interneurons (5HT3aR Re, VIP, *Lhx6*) and empty spiracles homeobox 1 (*Emx1*)-expressing pyramidal cells from P6 to P12 in the barrel cortex of unanesthetized pups (Figures 1A and 1B; Figure S1). Due to the scarcity of VIP interneurons in layer I (LI), the *5HT3aR.Cre* mouse line al-

lows for the selective analysis of non-VIP, 5HT3aR interneurons in this layer, approximately 81% of which express Re (Figures S2A–S2E).

To compare calcium activity among genetically labeled populations, we quantified event frequency and duration (Figures 1C–1F), as well as event synchrony, defined as the percentage of cell pairs that displayed significantly correlated activity out of all possible pairs (Figure 1G). We found that neurons in the somatosensory cortex showed prominent spontaneous calcium transients at P6, consistent with previous reports (Allène et al., 2008; Golshani et al., 2009). 5HT3aR Re interneurons showed infrequent events (Figures 1C–1E) that involved the majority of the cells within the field of view (FOV) (Figure 1D; Video S1) and exhibited significantly longer durations than other populations (Figure 1F). To ensure that our analysis reflected somatic events, we re-analyzed a subset of the movies using a previously described method for neuropil correction (Figures S2F and S2G; also see STAR Methods) (Peron et al., 2015). We found no significant differences in the frequency or correlation after applying the correction.

Our analysis revealed that 5HT3aR Re interneurons show significantly higher correlated activity than VIP and *Lhx6* interneurons (Figure 1G). To measure synchrony at the network level, we quantified the percentage of neurons that participate in network events (Figure 1H; also see STAR Methods for details). *Emx1* neurons exhibited more frequent calcium transients per cell than 5HT3aR Re and VIP interneurons (Figure 1E), and their activity was highly correlated between closely apposed cells (Figure 1I; Video S2). However, fewer *Emx1* neurons participated in large-scale synchronous events, which led to lower overall correlation (Figures 1G–1I). Thus, although pyramidal cells and interneurons both exhibit early activity, 5HT3aR Re interneurons show the highest degree of synchrony by the end of the first postnatal week. Therefore, we focused our study on the contribution of this activity pattern to the emergence of mature connectivity.

Figure 1. Cell-type-Specific Network Dynamics in the Developing Mouse Somatosensory Cortex In Vivo

- (A) Schematic representation of the imaging setup and cranial window location. Dextran staining (red) indicates the location of the cranial window. Scale bar, 500 μ m.
- (B) Schematic representation of the timeline for imaging sessions.
- (C) Representative raw $\Delta F/F$ traces for different neuronal types.
- (D) Representative images averaged from 500 frames in a single movie and corresponding rastergrams for detected calcium events in *5HT3aR.GCaMP6s*, *VIP.GCaMP6s*, *Lhx6.GCaMP6s*, and *Emx1.GCaMP6s* mice. Movies were taken at 50 μ m, 140 μ m, 130 μ m, and 150 μ m from the pial surface, respectively (also see Figure S2A). Each horizontal line in the rastergram represents a calcium event from onset to offset. Scale bar, 100 μ m.
- (E) Average event frequency in *5HT3aR.GCaMP6s* ($n = 14$ movies, 5 mice), *VIP.GCaMP6s* ($n = 14$ movies, 4 mice), *Lhx6.GCaMP6s* ($n = 6$ movies, 3 mice), and *Emx1.GCaMP6s* ($n = 10$ movies, 3 mice) mice. Event frequency was measured for each cell and averaged for all cells in a movie. One-way ANOVA ($p = 0.0012$) followed by Tukey's multiple comparisons test comparing between two genotypes; *5HT3aR.GCaMP6s* versus *Emx1.GCaMP6s*: $p = 0.0057$; *VIP.GCaMP6s* versus *Emx1.GCaMP6s*: $p = 0.0033$.
- (F) Average event duration. One-way ANOVA ($p = 0.001$) followed by Tukey's multiple comparisons test; *5HT3aR.GCaMP6s* versus *VIP.GCaMP6s*: $p = 0.019$; *5HT3aR.GCaMP6s* versus *Lhx6.GCaMP6s*: $p = 0.0043$; *5HT3aR.GCaMP6s* versus *Emx1.GCaMP6s*: $p = 0.0055$.
- (G) Percentage of neuronal pairs that exhibit significantly correlated activity as determined by Monte Carlo simulation of the number of all possible pairs. Kruskal-Wallis test ($p < 0.0001$) followed by Dunn's multiple comparisons test comparing between two genotypes; *5HT3aR.GCaMP6s* versus *VIP.GCaMP6s*: $p = 0.0001$; *5HT3aR.GCaMP6s* versus *Lhx6.GCaMP6s*: $p = 0.0016$; *5HT3aR.GCaMP6s* versus *Emx1.GCaMP6s*: $p = 0.0089$.
- (H) Average percentage of active neurons during network events. One-way ANOVA ($p = 0.0004$) followed by Tukey's multiple comparisons test; *5HT3aR.GCaMP6s* versus *VIP.GCaMP6s*: $p = 0.0002$; *5HT3aR.GCaMP6s* versus *Lhx6.GCaMP6s*: $p = 0.066$; *5HT3aR.GCaMP6s* versus *Emx1.GCaMP6s*: $p = 0.026$.
- (I) Average correlation coefficients of all cell pairs plotted against their binned distance in recordings from *Emx1.GCaMP6s* (red) and *5HT3aR.GCaMP6s* (black). Preferred model compared by the extra-sum-of-squares F test, *5HT3aR.GCaMP6s*: straight line; *Emx1.GCaMP6s*: exponential decay ($p < 0.0001$). *5HT3aR.GCaMP6s*: $n = 14$ movies, 5 mice; *Emx1.GCaMP6s*: $n = 10$ movies, 3 mice. ns: $p > 0.05$, * $p < 0.05$, ** $p < 0.01$, *** $p < 0.001$, **** $p < 0.0001$. Error bars indicate SEM. See also Figures S1–S4 and Videos S1 and S2.

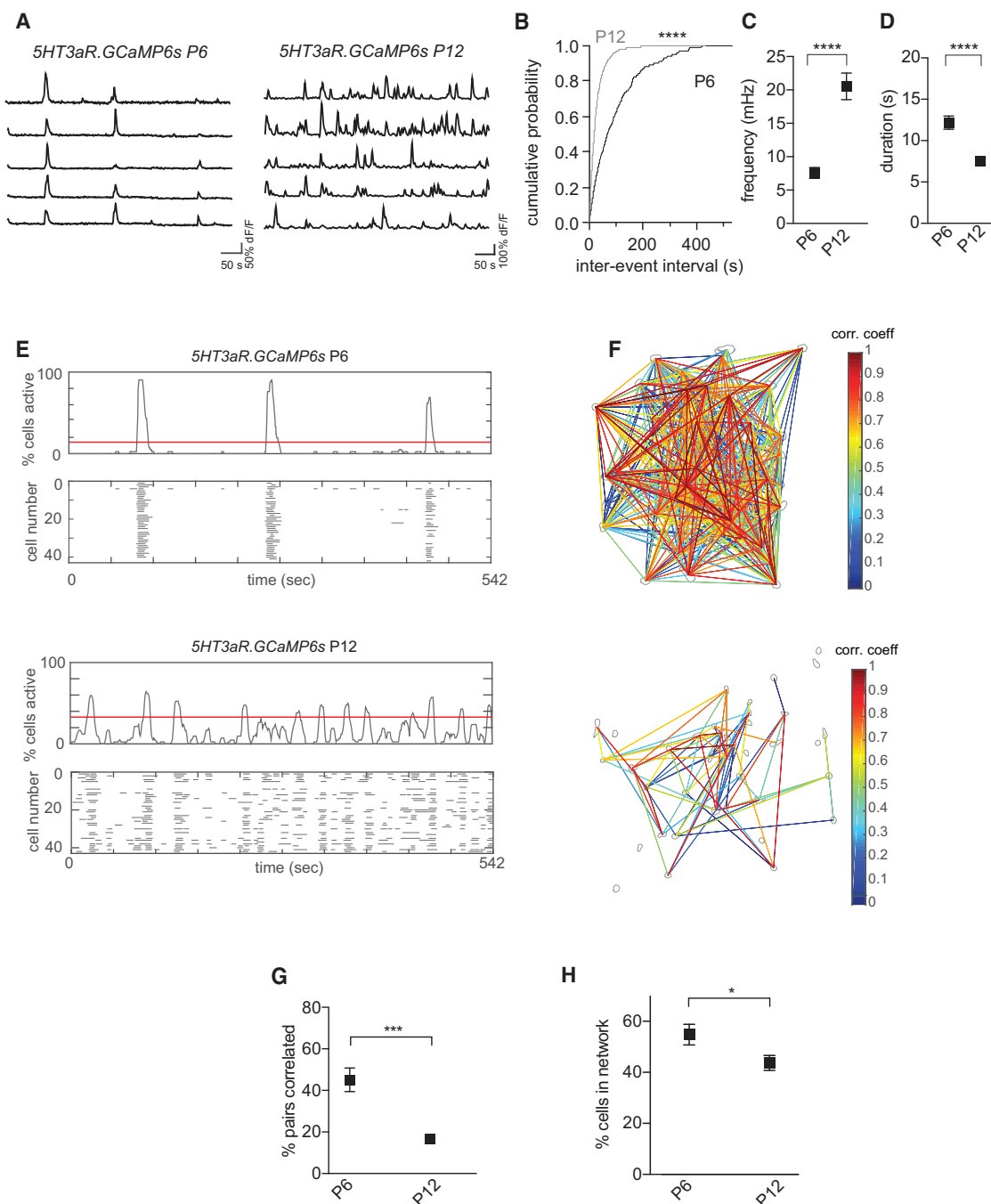


Figure 2. Developmental Desynchronization of Spontaneous Activity in 5HT3aR Re Interneurons

(A) Raw $\Delta F/F$ traces of five *5HT3aR.GCaMP6s* neurons from P6 and P12 movies.

(B) Cumulative probability plot of inter-event interval from all calcium events. Kolmogorov-Smirnov test, $p < 0.0001$.

(C) Mean event frequency in *5HT3aR.GCaMP6s* neurons at P6 ($n = 14$ movies, 5 mice) and P12 ($n = 11$ movies, 3 mice). Unpaired t test, $p < 0.0001$.

(D) Mean event duration per neuron in *5HT3aR.GCaMP6s* neurons at P6 and P12. Unpaired t test, $p < 0.0001$.

(E) Representative histograms of the percentage of active interneurons and corresponding event rastergrams for P6 (top) and P12 (bottom) recordings. Red lines on the histograms indicate the detection threshold for network events.

(F) Visualization of networks corresponding to recordings in (E). Gray contours represent somas within which calcium signals were analyzed. Lines connect cell pairs exhibiting significantly correlated activity. Line color indicates the magnitude of the correlation coefficient.

(G) Percentage of pairs exhibiting significantly correlated activity at P6 and P12. Unpaired t test, $p = 0.0002$.

(H) Average percentage of active cells during network events. The percentage of cells active per network event corresponds to the peak of that event above the red threshold line (E). Unpaired t test, $p = 0.044$. * $p < 0.05$, *** $p < 0.001$, **** $p < 0.0001$. Error bars indicate SEM. See also [Figures S3](#) and [S5](#).

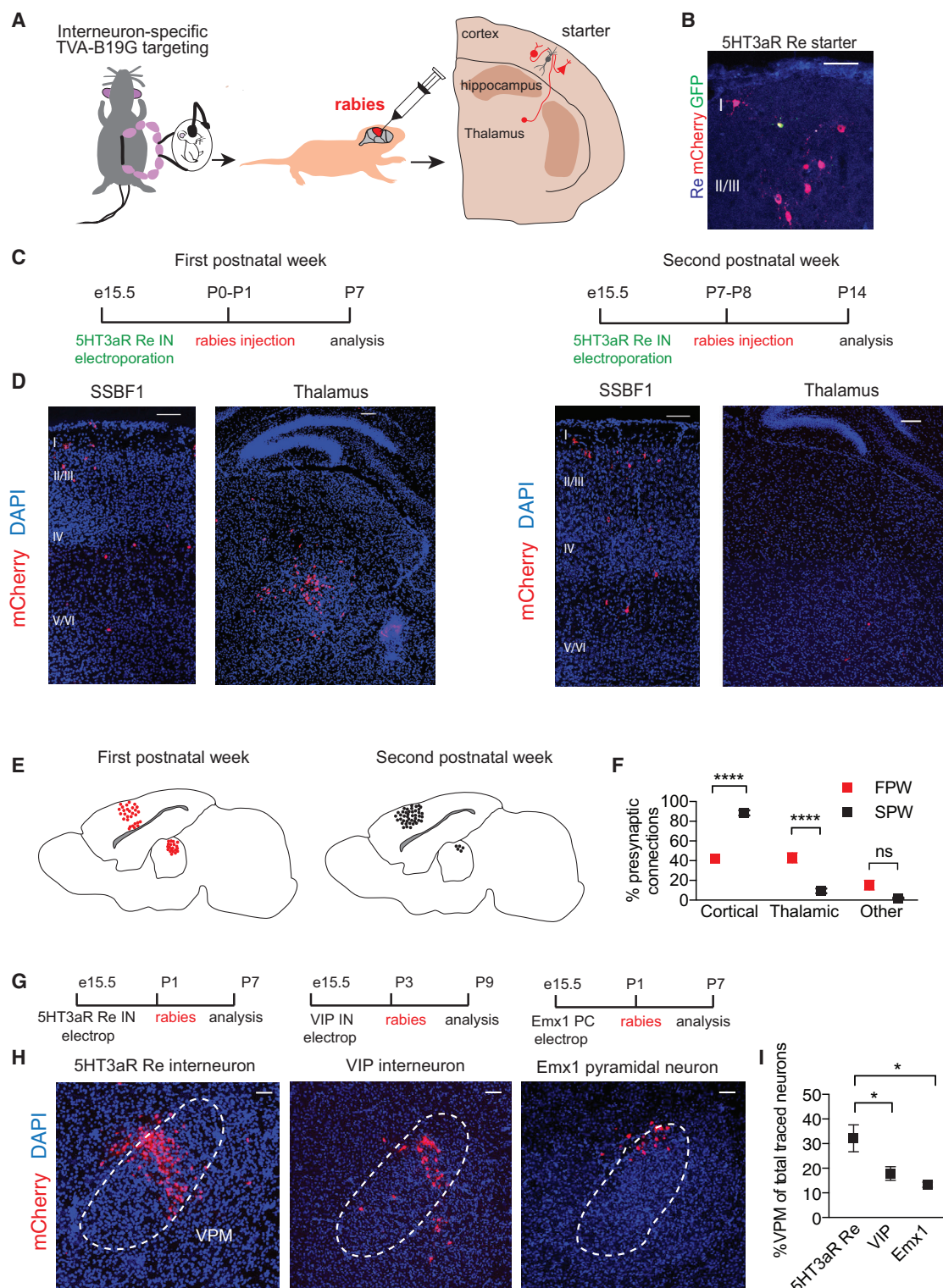


Figure 3. Temporal Regulation of Thalamic Inputs to 5HT3aR Re Interneurons

(A) Schematic representation of the experimental strategy for rabies monosynaptic tracing.

(B) Representative example of a reelin-expressing (blue) starter cell labeled by eGFP (green) and mCherry (red) expression.

(C) Schematic representation of the experimental timeline.

(legend continued on next page)

5HT3aR Re Interneuron Activity Becomes Decorrelated during Development

Since spontaneous correlated activity is rarely observed in the mature somatosensory cortex (Clancy et al., 2015; Peron et al., 2015), we next determined whether 5HT3aR Re interneuron activity changes as development proceeds. We focused our analysis on the transition from the first to the second postnatal week, a period critical for the maturation of somatosensory circuits (Chittajallu and Isaac, 2010; Fox, 1995) (Figure 2). Although we detected similar numbers of active 5HT3aR Re interneurons at P6 and P12 (Figure S3E), we found significant differences in their activity patterns. Despite an increase in the frequency of calcium events per cell (Figures 2A–2C), fewer cell pairs exhibited correlated activity at P12 (Figures 2E–2G). In addition, event duration decreased with age (Figure 2D). At a network level, significantly fewer cells were involved in co-active events at P12 (Figure 2H). These results indicate that 5HT3aR Re interneurons go through robust developmental desynchronization from the first to the second postnatal week. Whereas such decorrelation (Figure S5) has been shown to be independent of sensory inputs in pyramidal cell development (Golshani et al., 2009), it is unclear whether extrinsic inputs or intrinsic cellular processes mediate desynchronization in interneurons. Since we have previously shown that superficial 5HT3aR Re interneurons receive both local and long-range connectivity in the first postnatal week (De Marco García et al., 2015), we assessed whether changes in their connectivity pattern may underlie developmental desynchronization.

Thalamic Innervation to Superficial Interneurons Is Dynamically Remodeled at Neonatal Stages

To identify developmental changes in connectivity, we mapped monosynaptic inputs onto 5HT3aR Re interneurons during two consecutive postnatal periods. To this end, we first electroporated 5HT3aR Re interneurons with a *Dlx5/6-hGFP-TVA-B19G* plasmid at embryonic day 15.5 (E15.5), a stage when CGE interneuron production is maximal (De Marco García et al., 2011) (Figure 3). Next, we injected a recombinant rabies virus (*SADΔG_mCherry(EnvA)*) into the somatosensory barrel field 1 area (SSBF1) at P0–P1 or P7–P8 and analyzed presynaptic inputs at P7 or P14, respectively (Figures 3A–3C). Similar to our previous findings, a significant proportion of inputs to 5HT3aR Re interneurons originate in the ventroposteromedial thalamic nucleus (VPM) at P7 despite the superficial position of their somata (Figures 3D–3F; also see De Marco García et al., 2015). Although neither the number of starter cells nor the number of inputs per

cell was significantly different between P7 and P14 (Figures S6A and S6B), thalamic inputs decreased from $42.96\% \pm 5.05\%$ to $9.46\% \pm 2.42\%$, while cortical inputs increased from $41.80\% \pm 3.31\%$ to $88.54\% \pm 2.60\%$ (Figures 3E and 3F). Together, these results indicate that superficial 5HT3aR Re interneurons receive substantial functional inputs from the thalamus during the first postnatal week. These inputs are significantly reduced by the second postnatal week.

To determine whether VPM innervation is also prominent among other superficial neurons in the first postnatal week, we selectively mapped the afferent connectivity of VIP and Emx1 neurons in layers II/III. We electroporated a *pAAV-EF1a-FLEX-GTB* construct at E15.5 in *VIP^{Cre}* or *Emx1^{Cre}* mice (Figure 3G; Table S3). Rabies virus was injected at P3, and brains were analyzed at P9 for *VIP^{Cre}* mice to ensure a sufficient level of Cre recombinase at the time of injection (Figure 3G). We found that the proportion of inputs originating in the VPM was significantly larger for 5HT3aR Re interneurons compared to VIP interneurons and pyramidal cells (Figures 3H and 3I). Altogether, these results indicate that within superficial cortical layers, 5HT3aR Re interneurons are the preferred targets of VPM input at P7–P9 (Figure S6I).

5HT3aR Re Interneurons Are Recruited by Whisker Stimulation at Neonatal Stages

As the decrease in thalamic innervation parallels the time course of network desynchronization, and our previous work indicates that these inputs are fundamental for interneuron maturation (De Marco García et al., 2015), we focused our study on the contribution of thalamo-cortical connectivity to the emergence of interneuron-specific activity patterns. To do this, we selectively targeted expression of GCaMP6s to thalamic neurons using *SERT^{Cre}* mice (Figure 4). The serotonin transporter is transiently expressed in thalamic neurons during development, and thus, the *SERT^{Cre}* driver line allows for the targeting of these neurons and their terminals (Narboux-Nême et al., 2008; Pouchelon et al., 2014). Activity patterns in thalamic axonal arbors were analyzed as regions of interest (ROIs) by applying a grid over the images obtained from calcium recordings (Ackman et al., 2012; Peron et al., 2015). We found that terminals present in LI exhibited similar inter-event intervals (Figures 4A–4D) and event frequency (Figure 4E) as those of 5HT3aR Re interneurons at P6. These events became decorrelated at P11 (Figure 4B).

The similar temporal dynamics of calcium transients in thalamic terminals and interneurons, as well as the presence of functional monosynaptic contacts between these circuit

(D) Representative example of presynaptic partners to 5HT3aR Re interneurons in the somatosensory barrel field (SSBF1) and the thalamus during the first (left) and second (right) postnatal weeks.

(E) Schematic representation of presynaptic connectivity to 5HT3aR Re interneurons. Each dot represents a traced presynaptic neuron.

(F) Proportion of presynaptic inputs to 5HT3aR Re interneurons across brain regions in the first postnatal week (FPW) ($n = 5$ mice) and second postnatal week (SPW) ($n = 7$ mice). Two-way ANOVA after arcsine transformation followed by Bonferroni's multiple comparisons test. FPW versus SPW: cortical, $p < 0.0001$; thalamic $p < 0.0001$.

(G) Schematic representation of experimental procedures used to trace 5HT3aR Re, VIP, and pyramidal cells (PCs) (also see Table S3).

(H) VPM monosynaptic connectivity originating from 5HT3aR Re interneurons (left), VIP interneurons (middle), and pyramidal neurons (right).

(I) Proportion of VPM inputs over the total number of inputs to superficial neurons (5HT3aR Re: $n = 5$ mice, VIP: $n = 5$ mice, Emx1: $n = 3$ mice). Unpaired t test, 5HT3aR Re versus VIP: $p = 0.48$; 5HT3aR Re versus Emx1: $p = 0.043$. * $p < 0.05$, **** $p < 0.0001$, ns: $p > 0.05$. Error bars indicate SEM. Scale bar, 100 μm . See also Figure S6 and Table S3.

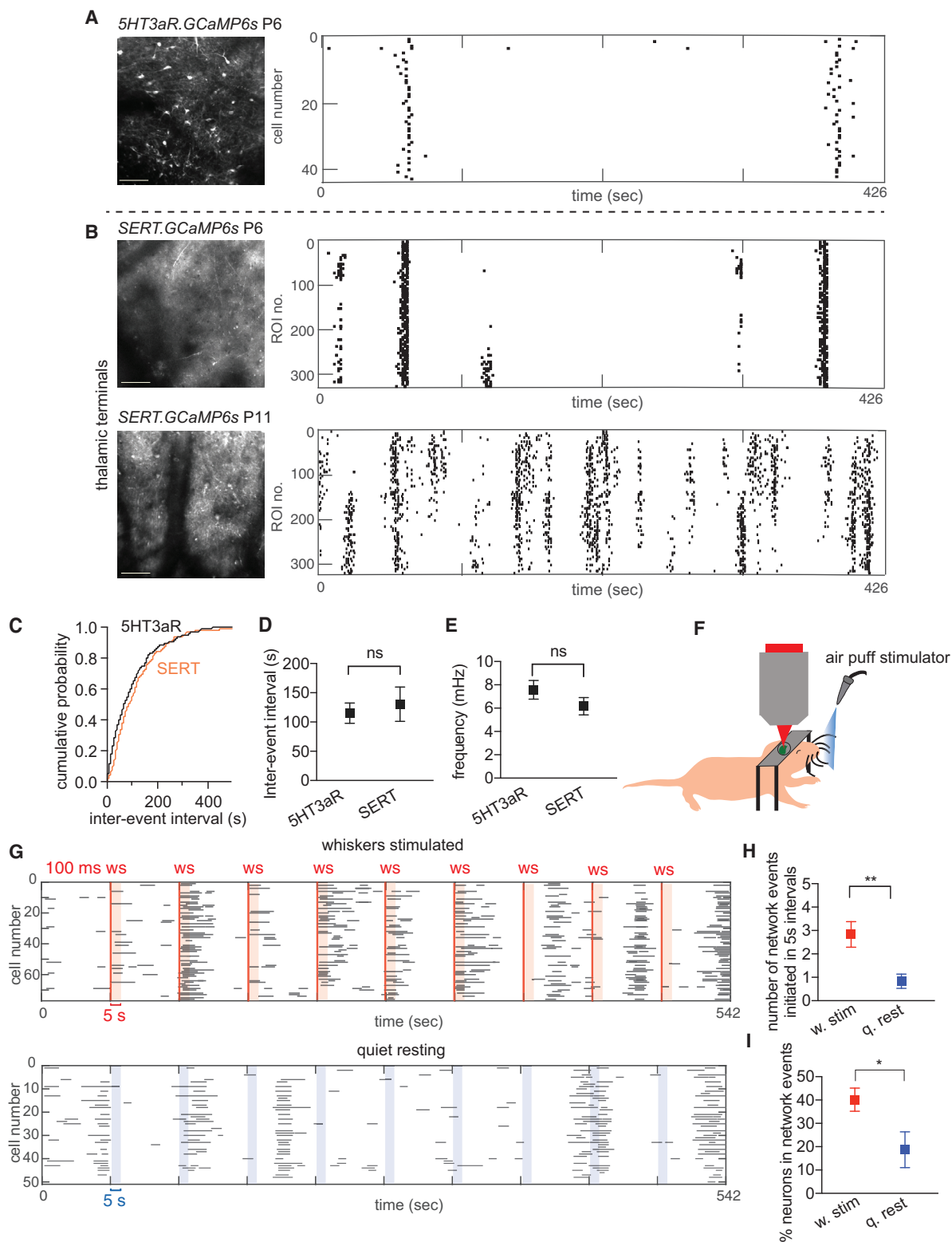


Figure 4. Whisker Stimulation Activates 5HT3aR Re Interneurons at P6

(A) Sample image and corresponding onset rastergram of calcium events in *5HT3aR.GCaMP6s* mice at P6. Each black square indicates event onset. Imaging depth was 50 μ m from pial surface.

(legend continued on next page)

components (Figure S6), led us to ask whether sensory stimulation activated superficial interneurons at this stage. To test this, we applied air puffs to stimulate all whiskers unilaterally and imaged the contralateral barrel cortex in *5HT3aR.GCaMP6s* mice at P6 (Figure 4F). Air puffs (100 ms) were triggered by the onset of the laser scan every 50 frames. We quantified the number of network events initiated immediately after each stimulation (event peak within 5 s after stimulation) and the percentage of cells involved in these network events (Figures 4G–4I). For comparison, we quantified network events in equivalent frames during recordings while the same animal was resting and no air puff was applied. We observed significantly more network events after whisker stimulation than during quiet resting (Figure 4H). In addition, the percentage of cells participating in these network events was significantly higher in the stimulated condition (Figure 4I). These results indicate that 5HT3aR Re interneurons are activated by sensory stimulation at neonatal stages.

Sensory Deprivation Decorrelates Interneuron but Not Excitatory Network Activity

Given that sensory inputs effectively activate 5HT3aR Re interneurons in the first postnatal week, we assessed whether they contribute to the correlated activity observed. We performed calcium imaging in *5HT3aR.GCaMP6s* mice subjected to chronic whisker plucking (Figure 5). We found that sensory deprivation led to a significant decrease in the percentage of correlated pairs (Figures 5A, 5B, and 5D) as well as the percentage of interneurons participating in network events by P6 (Figure 5E). Consistent with previous observations (Golshani et al., 2009), we show that event frequency and duration, as well as network correlation, in genetically defined excitatory neurons are not altered by sensory deprivation (Figures 5C–5G). Thus, perturbation of sensory inputs leads to loss of synchrony selectively in 5HT3aR Re interneurons at P6. These defects are long lasting, as both network synchrony and event frequency are not significantly different from P6 to P12 in sensory-deprived mice (Figures 5H and 5I). These results suggest that thalamic inputs contribute to the emergence of synchronous activity in developing interneurons.

Despite inducing a reduction in interneuron synchronization, sensory deprivation led to a significant increase in the frequency of calcium transients (Figure 5F) but no change in event duration at P6 (Figure 5G). The increase in event frequency in 5HT3aR Re interneurons may be a network effect resulting from weakened thalamic inputs to all cell types across cortical layers after sen-

sory deprivation. As sensory deprivation could impact both monosynaptic and polysynaptic inputs onto developing interneurons, we next performed imaging experiments on mice in which thalamocortical inputs onto 5HT3aR Re interneurons were genetically altered.

Developmental Attenuation of NMDAR Signaling Perturbs the Co-activation of 5HT3aR Re Interneurons

To determine the circuit mechanism underlying interneuron synchronization, we carried out a genetic ablation of NMDARs by crossing *5HT3aR.Cre* with *NR1^{fl/fl}* mice (Figure 6). Our previous work indicates that NMDARs are enriched in thalamocortical synapses onto 5HT3aR Re interneurons whereas intracortical synapses display a large AMPA component (De Marco García et al., 2015). Although NMDAR-mediated currents were not eliminated, we found a significant reduction in the NMDA/AMPA ratio in NMDAR-ablated interneurons (Figures 6A and 6B). Despite a significant knockdown of NMDAR-dependent currents, 5HT3aR Re interneurons showed late spiking patterns and synaptic properties characteristic for these cells (Figures 6C and 6D; Table S4). In contrast to the effects of early NR1 removal by *in utero* electroporation (De Marco García et al., 2015), this strategy did not cause morphological defects in 5HT3aR Re interneurons (Figures 6E–6I). This apparent discrepancy in the effect of NMDAR loss of function on morphological development may be due to differences in the timing of ablation and/or the presence of residual NMDAR currents in *5HT3aR.Cre, NR1^{fl/fl}* mice. In addition, neither the migration nor the survival of 5HT3aR Re interneurons is affected by this manipulation (Figures S7A–S7C).

To assess whether NMDAR knockdown impacts the emergence of 5HT3aR Re interneuron network activity, we analyzed calcium dynamics in *5HT3aR.Cre, NR1^{fl/fl}.GCaMP6s* mice. We used *5HT3aR.Cre, NR1^{fl/+}.GCaMP6s* littermates as controls, since these mice showed activity dynamics indistinguishable from those of *5HT3aR.GCaMP6s* mice (% pairs correlated, Mann-Whitney test, $p = 0.32$; *5HT3aR.Cre, NR1^{fl/+}.GCaMP6s*: $n = 7$ movies; *5HT3aR.GCaMP6s*: $n = 14$ movies). Similar to the effect of sensory deprivation on network synchrony, NMDAR knockdown in 5HT3aR Re interneurons led to a significant reduction in the percentage of correlated pairs (Figures 6J and 6K) as well as in the proportion of cells participating in network events at P6 (Figure 6L). In contrast, event frequency and duration (Figures 6M and 6N) remained unaffected after NMDAR knockdown. These experiments show that sufficient activation

(B) Sample image and corresponding rastergrams of calcium events in thalamic axons of *SERT.GCaMP6s* mice at P6 (top) and P11 (bottom). Imaging depth was 50 μm from pial surface.

(C) Cumulative probability plot of inter-event intervals in *5HT3aR.GCaMP6s* (black) and *SERT.GCaMP6s* (orange) mice at P6.

(D) Average inter-event interval in *5HT3aR.GCaMP6s* ($n = 14$ movies, 5 mice) and *SERT.GCaMP6s* ($n = 6$ movies, 3 mice) mice. Mann-Whitney test, $p = 0.21$.

(E) Average frequency of calcium events. Mann-Whitney test, $p = 0.28$.

(F) Schematic representation of air puff stimulation setup. 100 ms air puffs were applied to stimulate whiskers on one side of the snout. Imaging was performed on the contralateral side.

(G) Representative rastergrams after whisker stimulation (w. stim, top) and quiet resting (q. rest, bottom). Red vertical lines mark the onsets of whisker stimulation (WS), and evoked events were quantified during the windows depicted by red shaded areas. Blue shaded areas indicate matching time windows for network event analysis in the quiet resting condition with no stimulation applied. Each line in rastergram represents the time course of a calcium event.

(H) Number of network events that occurred in the 5 s windows immediately after each whisker stimulation in 9-min movies (whisker stimulated: $n = 6$ movies, 4 mice) or in the same windows without stimulation (quiet resting control: $n = 6$ movies, 5 mice). Unpaired t test, $p = 0.0094$.

(I) Percentage of active neurons in each network event. Unpaired t test, $p = 0.041$. * $p < 0.05$, ** $p < 0.01$, ns: $p > 0.05$. Error bars indicate SEM. Scale bar, 100 μm .

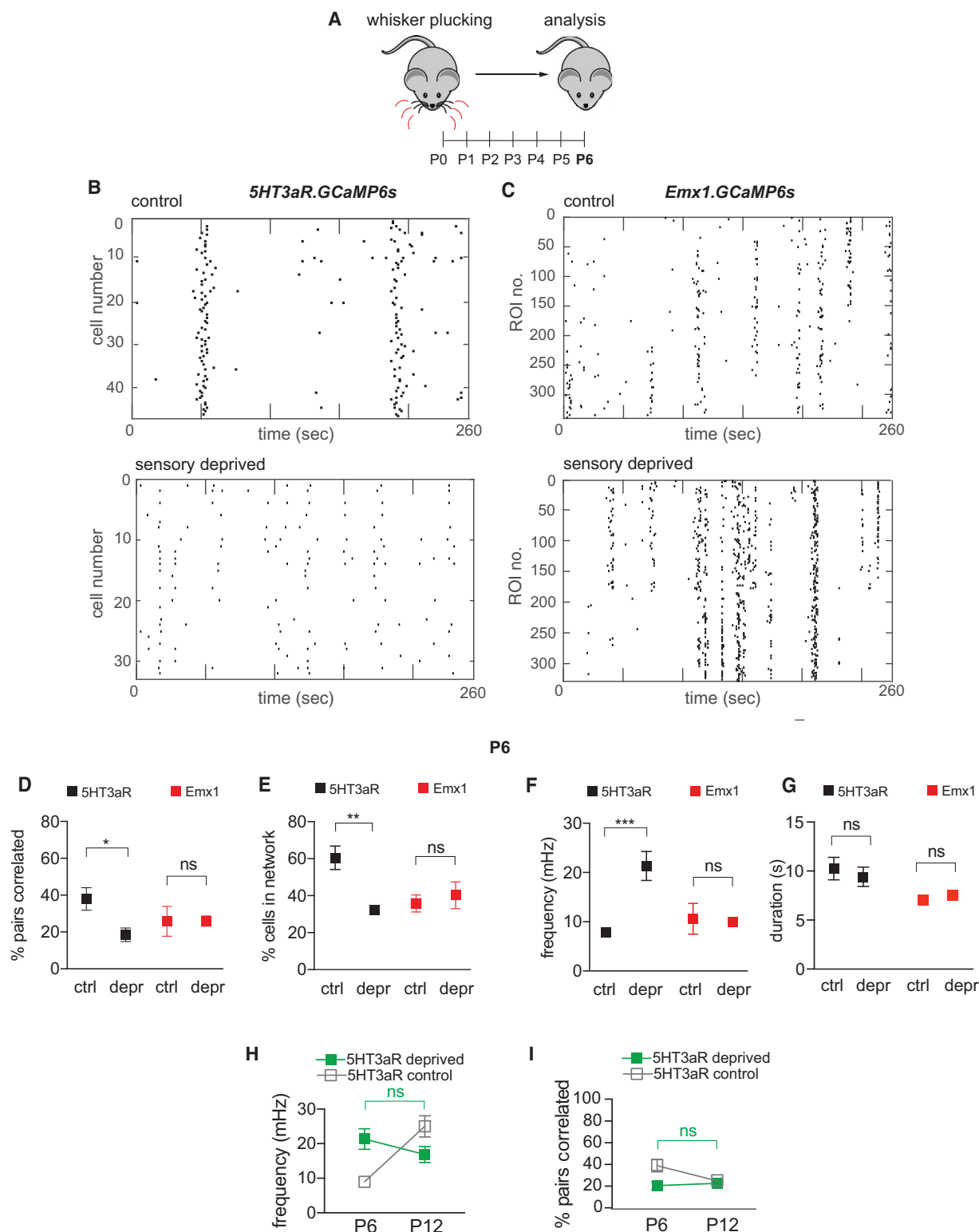


Figure 5. Sensory Deprivation Causes Persistent Desynchronization of 5HT3aR Re, but Not Emx1 Neurons

(A) Schematic representation of the experimental strategy for sensory deprivation.

(B and C) Representative rastergrams showing the onset of calcium events for control (B, top) and sensory-deprived (B, bottom) neurons recorded in *5HT3aR.GCaMP6s* at P6 and *Emx1.GCaMP6s* mice at P6 (C).

(legend continued on next page)

of NMDARs is fundamental for the emergence of synchronous network patterns in 5HT3aR Re interneurons.

Dampening of Thalamic Inputs to 5HT3aR Re Interneurons Causes Aberrant Activation of Superficial Pyramidal Cells

Since superficial 5HT3aR Re interneurons innervate layer II/III pyramidal cells in mature animals (Cruikshank et al., 2012; Jiang et al., 2015, 2013; Lee et al., 2015; Wozny and Williams, 2011) and can inhibit a large number of neurons via volume transmission (Oláh et al., 2007; Overstreet-Wadiche and McBain, 2015), we hypothesized that they could contribute to sensory map formation by inhibiting spontaneous activity in pyramidal cells. To test this hypothesis, we first determined whether 5HT3aR Re interneurons synapse onto layer II/III pyramidal cells by the end of first postnatal week (Figure 7). Rabies tracing of layer II Emx1 neurons revealed the presence of anatomical connectivity from LI interneurons (Figures 7A and 7B), and optogenetic activation of LI interneurons elicited detectable monosynaptic inhibitory responses in these cells (Figures 7C and 7D).

We then surveyed pyramidal cell activity in *5HT3aR.Cre*, *NR1^{fl/fl}* mice, in which superficial interneuron networks are dysfunctional. To target possible postsynaptic partners of 5HT3aR Re interneurons, we injected an AAV1.syn.GCaMP6s.WPRE.SV40 virus in control *NR1^{fl/fl}* and *5HT3aR.Cre*, *NR1^{fl/fl}* mice at P0 and analyzed calcium responses to whisker stimulation at P7 (Figures 7E and 7F). Previous reports suggest that this viral approach largely targets excitatory cells (96%) in layer II/III and only a small fraction of GABAergic interneurons (4%) (Peron et al., 2015). In both *5HT3aR.Cre*, *NR1^{fl/fl}* and control mice, we detected similar numbers of active neurons per FOV, suggesting that the viral infection was consistent across experiments and genotypes (Figure S7D).

To evoke sensory responses, we applied air puffs onto the whiskers as described before (Figures 4F and 7E). We found that sensory stimulation evoked a higher rate of network events (Figures 7G and 7H) and a larger number of participating neurons per event in *5HT3aR.Cre*, *NR1^{fl/fl}* mice compared to controls without affecting spontaneous events (Figure 7I; Figures S8A–S8C). Moreover, the correlation between distant cell pairs was consistently higher in *5HT3aR.Cre*, *NR1^{fl/fl}* as compared to control mice, suggesting that co-active neurons occupy larger areas in mutant mice (Figure 7J). In addition, the small fraction of LI interneurons that were also labeled by viral infection of the same mice showed a markedly lower number of network events

evoked by whisker stimulation (Figures S8D–S8F), indicating that the thalamic recruitment of 5HT3aR Re interneurons was impaired in *5HT3aR.Cre*, *NR1^{fl/fl}* mice. These results suggest that the co-activation of 5HT3aR Re interneurons restricts pyramidal cell activation during sensory stimulation.

NMDAR Ablation in 5HT3aR Re Interneurons Leads to Enlarged Barrels and Impaired Whisker-Dependent Texture Discrimination

To assess whether aberrant activation of pyramidal cells leads to anatomical defects, we analyzed the barrel map in the somatosensory cortex (Figures 8A–8I). We found a 14% expansion in the total barrel area, defined as the sum of all individual barrels (Figures 8A and 8B). Specifically, rows A, B, D, and E were significantly larger in *5HT3aR.Cre*, *NR1^{fl/fl}* mice (Figure 8C). To further determine whether the expansion of thalamic terminals is accompanied by changes in cell numbers in barrels or septa, we quantified cell density, septal width, and barrel/septal boundary in row D of control and *5HT3aR.Cre*, *NR1^{fl/fl}* mice at P8 (Miceli et al., 2013) (Figures 8D–8H). *5HT3aR.Cre*, *NR1^{fl/fl}* mice had significantly smaller septa and sharper barrel/septal boundaries than controls (Figures 8G–8I). In contrast, cell density was unchanged in mutant mice (Figure 8F). These results indicate that barrel enlargement in *5HT3aR.Cre*, *NR1^{fl/fl}* mice may reflect denser thalamic projections in the septal wall and/or ectopic axonal invasion of the septal space. These results are consistent with an inhibitory role of 5HT3aR Re interneurons in sharpening columnar organization in the barrel cortex.

To determine whether deletion of NMDARs in 5HT3aR Re interneurons has a long-lasting impact on behavior, we evaluated the performance of *5HT3aR.Cre*, *NR1^{fl/fl}* mice in a whisker-dependent texture discrimination task at P40–P50 (Che et al., 2016; Chen et al., 2017; Wu et al., 2013) (Figure 8J). We found that NR1 knockdown in 5HT3aR Re interneurons leads to an impairment in tactile discrimination but not in exploratory behavior (Figures 8K and 8L). Although VIP interneurons are also targeted by the *5HT3aR.Cre* driver line, we hypothesize that these neurons likely do not significantly contribute to the observed effects, since they have a significantly lower NMDAR/AMPA ratio (Figure S7E) and receive significantly fewer VPM inputs compared to the 5HT3aR Re population (Figures 3H and 3I). Together, these results indicate that early dysfunction of 5HT3aR Re interneurons leads to deficits in barrel map formation and long-lasting behavioral defects.

(D) Percentage of correlated pairs in *5HT3aR.GCaMP6s* and *Emx1.GCaMP6s* mice in control and deprived conditions at P6 (*5HT3aR* control: *n* = 5 movies, 3 mice; deprived: *n* = 6 movies, 3 mice. *Emx1* control: *n* = 5 movies, 3 mice; deprived *n* = 8 movies, 3 mice). *5HT3aR.GCaMP6s* control versus deprived: *p* = 0.03; *Emx1.GCaMP6s* control versus deprived: *p* > 0.99.

(E) Percentage of neurons in network events at P6. *5HT3aR.GCaMP6s* control versus deprived: *p* = 0.0017; *Emx1.GCaMP6s* control versus deprived: *p* > 0.99. (F and G) Average event frequency (F, *5HT3aR.GCaMP6s* control versus deprived: *p* = 0.0007; *Emx1.GCaMP6s* control versus deprived: *p* > 0.99) and event duration (G, *5HT3aR.GCaMP6s* control versus deprived: *p* = 0.86; *Emx1.GCaMP6s* control versus deprived: *p* > 0.99) at P6.

(H) Quantification of event frequency in *5HT3aR.GCaMP6s* mice from P6 to P12. (P6 control: *n* = 5 movies, 3 mice; deprived: *n* = 6 movies, 3 mice. P12 control: *n* = 7 movies, 3 mice; deprived *n* = 7 movies, 2 mice). P6 versus P12: control, *p* = 0.0008, deprived: *p* = 0.46. Significance of P6 versus P12 comparison in sensory-deprived condition is indicated on the graph.

(I) Percentage of neuronal pairs undergoing correlated activity in sensory-deprived and control *5HT3aR.GCaMP6s* neurons from P6 to P12. P6 versus P12: control, *p* = 0.05; sensory deprived, *p* > 0.99. Significance of P6 versus P12 comparison in sensory-deprived condition is indicated on the graph.

Two-way ANOVA followed by Bonferroni's multiple comparisons test for all comparisons. **p* < 0.05, ***p* < 0.01, ****p* < 0.001, ns: *p* > 0.05. Error bars indicate SEM.

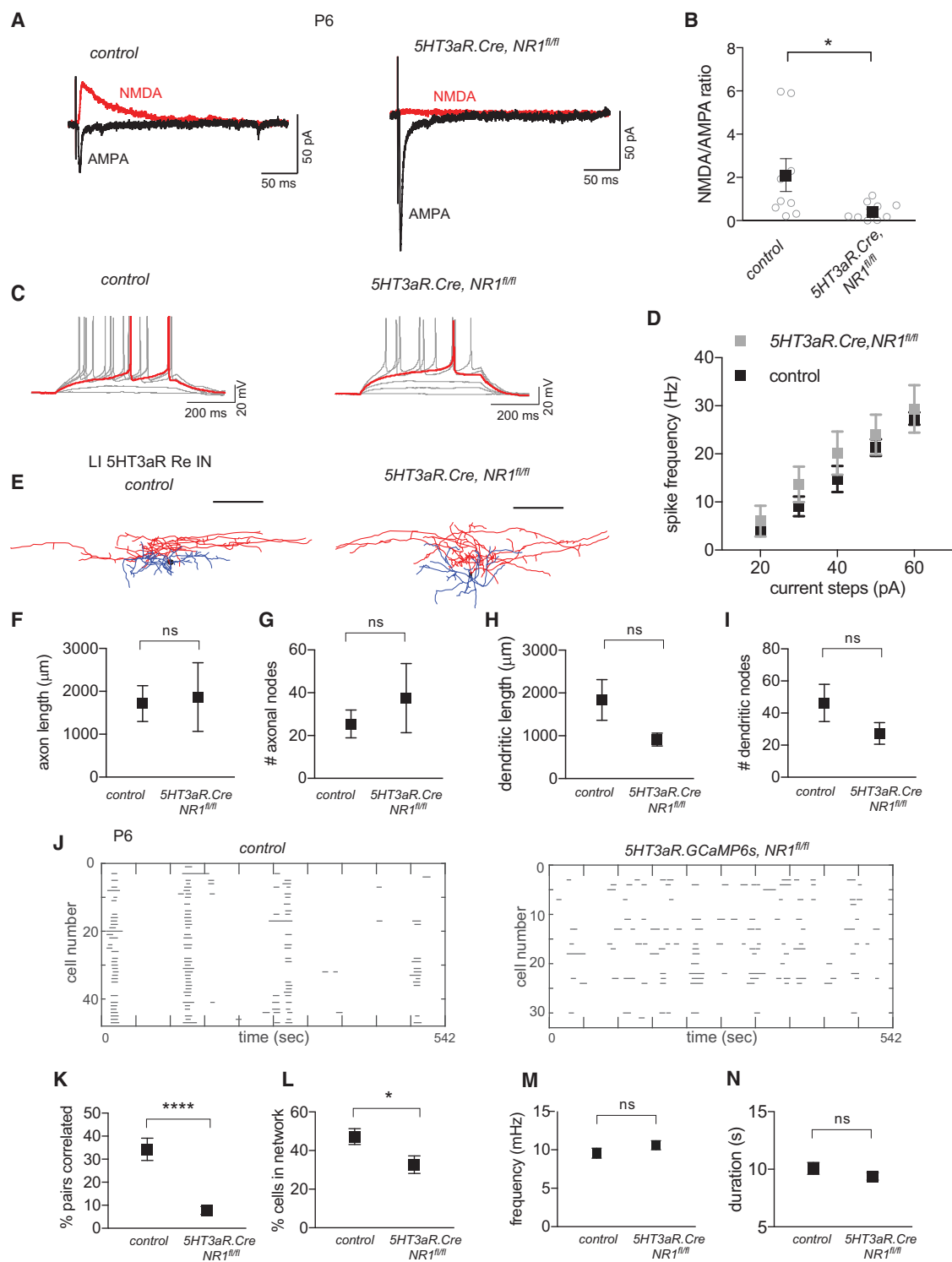


Figure 6. NMDAR Knockdown in 5HT3aR Re Interneurons Disrupts Network Synchrony

(A) Average evoked EPSCs mediated by NMDARs (red) and AMPARs (black) in 5HT3aR Re interneurons in control NR1^{fl/fl} (left) and 5HT3aR.Cre, NR1^{fl/fl} (right) neurons.
 (B) NMDA-to-AMPA ratios for 5HT3aR Re interneurons in control (n = 9 neurons) and 5HT3aR.Cre, NR1^{fl/fl} (n = 9 neurons) mice. Black squares indicate average ratios, and open circles indicate individual values. Mann-Whitney test, p = 0.014.

(legend continued on next page)

DISCUSSION

Despite a growing recognition of the prominent role that interneurons play in the processing of sensory information in the adolescent and mature brain (Batista-Brito et al., 2017; Cardin et al., 2009; Isaacson and Scanziani, 2011; Karnani et al., 2016), it is unclear whether networks of select interneuron types are recruited during early development. Progress in the study of maturing networks has been hampered, in part, by technical difficulties in tracking neuronal activity longitudinally at neonatal stages. Pioneering approaches in the study of neonatal cortical rhythms focused on short-term multiunit recordings and imaging using voltage-sensitive or calcium affinity dyes (Garaschuk et al., 2000; Golshani et al., 2009; Minlebaev et al., 2011; Yang et al., 2013). Although these approaches provided great insight to our understanding of global patterns of brain activity and activity-dependent development, they have limited cell-type resolution. This limitation has disproportionately affected the study of interneurons, which represent only 20%–30% of the total neuronal population yet exhibit prominent diversity (Markram et al., 2004; Ascoli et al., 2008). Our chronic cranial window preparation in combination with genetically targeted GCaMP6s expression to interneuron cell types enabled us to image the activity of neuronal populations as they mature.

Our results indicate that the somatosensory thalamus is a major source of long-range inputs to 5HT3aR Re interneurons in the barrel cortex during the first postnatal week. In contrast, neuromodulatory inputs to this population, such as those from the dorsal raphe and the nucleus basalis are not prominent at this age and mature later. Furthermore, the extent of VPM innervation onto superficial layers varies across cell types as VIP interneurons and pyramidal cells receive significantly fewer VPM inputs than 5HT3aR Re interneurons at P7–P9. Previous evidence indicates that 5HT3aR Re interneurons rely on NMDARs for integrating long-range inputs (Chittajallu et al., 2017; De Marco García et al., 2015). We showed that NMDARs are enriched in thalamocortical synapses onto 5HT3aR Re interneurons and that thalamic inputs constitute the most significant source of glutamatergic inputs to these neurons early in development. In agreement with these observations, attenuation of thalamic drive through removal of NMDARs desynchronizes 5HT3aR Re neuronal activity. In NMDAR-ablated 5HT3aR Re interneurons,

the lack of synchronization persists until P12, suggesting that synchrony in this population is disrupted and not delayed. Given the requirement of NMDARs for early synchronization, the reported network patterns in the 5HT3aR Re population cannot be explained solely by the presence of gap junctions. In support of this notion, less than 14% of interneurons in LI are connected via gap junctions at P6 (Yao et al., 2016). In addition, the proportion of electrically coupled interneurons increases to about 50% by P14 (Yao et al., 2016) during the same period in which 5HT3aR Re interneurons drastically desynchronize (Figure 2).

Could the desynchronization of thalamic-mediated interneuron activity be explained by a secondary effect from the deregulation of other synaptic inputs? One possibility is that changes in GABA signaling could be responsible for desynchronization. Since GABA-mediated synaptic events are present in NMDAR-ablated 5HT3aR Re interneurons (De Marco García et al., 2015), we think this possibility is unlikely. Another possibility is that inputs originating in the subplate may contribute to the de-synchronization of 5HT3aR Re interneurons. Indeed, subplate neurons exert significant influence on the maturation of inhibitory circuits in deep layers of sensory cortices (Kanold and Shatz, 2006; Tolner et al., 2012). Although our rabies virus tracing experiments revealed subplate innervation onto superficial 5HT3aR Re interneurons at P7 (Figure 3E), optogenetic mapping showed a significantly lower NMDA/AMPA ratio in intracortical compared to thalamocortical synapses. In addition, a similar number of subplate inputs is observed after NMDAR ablation in 5HT3aR Re interneurons (De Marco García et al., 2015). Thus, it is unlikely that the desynchronization of interneuron activity in *5HT3aR.Cre, NR1^{fl/fl}* mice is a consequence of abnormal subplate inputs onto these interneurons.

Our data show that activation of 5HT3aR Re neurons restricts the activation of upper layer excitatory neurons during sensory stimulation and refines the barrel map. These results point to an inhibitory role of GABA in the functional and structural establishment of developing somatosensory circuits. Although GABA acts as a depolarizing neurotransmitter at the single-cell level during early postnatal development in slice preparations (Ben-Ari, 2002; Chen and Kriegstein, 2015; Valeeva et al., 2016), its action on network activity in the intact brain appears to be inhibitory during the first postnatal week (Kirmse et al., 2015; Valeeva et al., 2016). At these early stages, endogenous GABA exerts a

(C) Representative traces of voltage responses to 500 ms step current injection in current-clamp configuration of LI 5HT3aR Re interneuron from control (left) and *5HT3aR.Cre, NR1^{fl/fl}* (right) mice. The intrinsic firing properties of 5HT3aR Re interneurons in *5HT3aR.Cre, NR1^{fl/fl}* mice showed a stereotypical late spiking pattern.

(D) Input-output relationship between current inputs and spike frequencies. Two-way ANOVA followed by Tukey's multiple comparisons test, $p > 0.05$ for all current step comparisons between control ($n = 6$ cells) and *5HT3aR.Cre, NR1^{fl/fl}* ($n = 6$ cells).

(E) Neurolucida reconstructions for control (left) and *5HT3aR.Cre, NR1^{fl/fl}* (right) LI 5HT3aR Re interneurons. Axons are shown in red and dendrites in blue. Scale bar, 100 μm .

(F) Axonal length of LI 5HT3aR Re interneurons. Unpaired t test, $p = 0.86$, *5HT3aR.Cre, NR1^{fl/fl}*: $n = 6$ neurons; control: $n = 9$ neurons.

(G) Quantification of axonal nodes in LI 5HT3aR Re interneurons. Unpaired t test, $p = 0.44$.

(H) Dendritic length of 5HT3aR Re interneurons. Mann-Whitney test, $p = 0.18$.

(I) Quantification of dendritic nodes in LI 5HT3aR Re interneurons. Mann-Whitney test, $p = 0.26$.

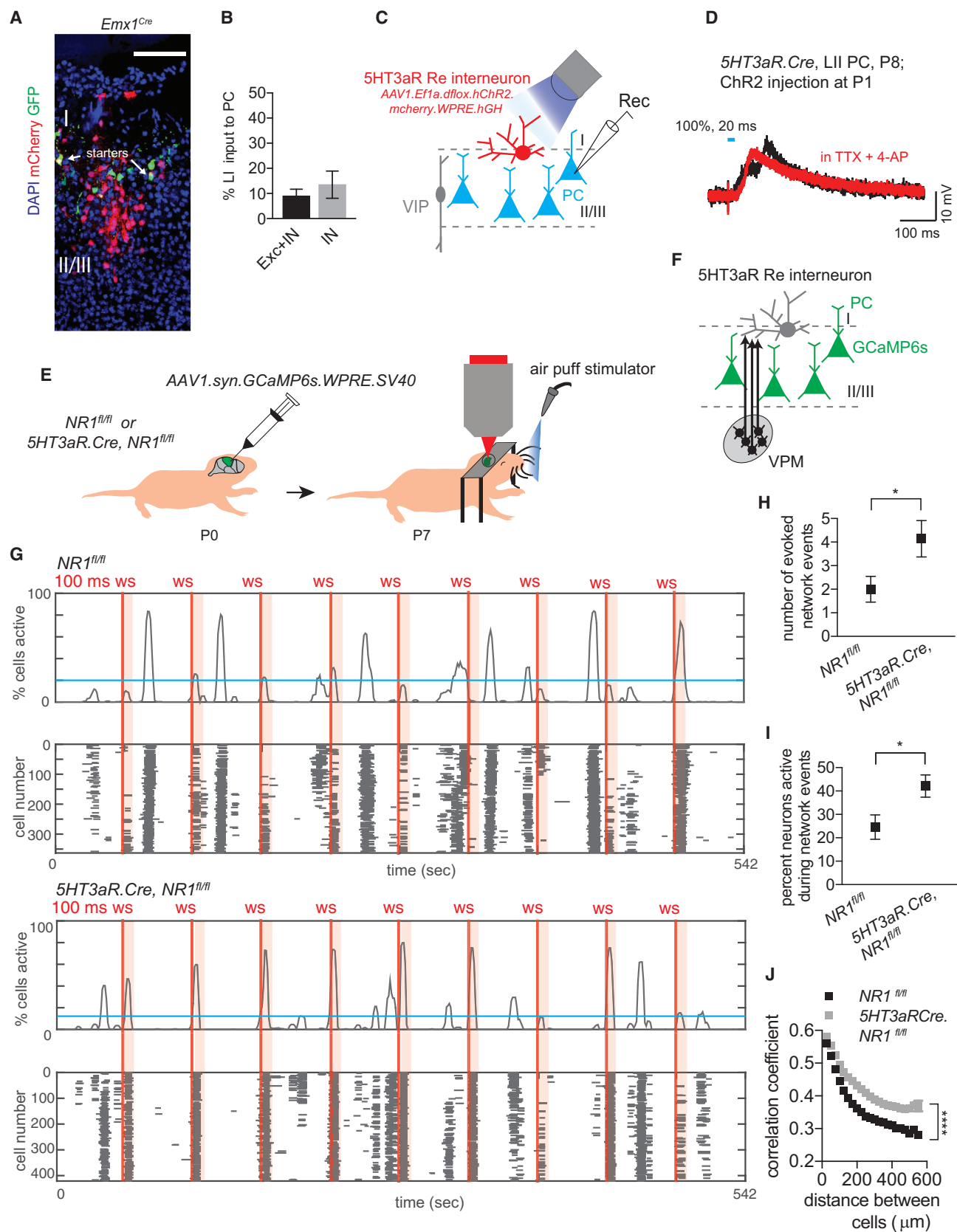
(J) Representative rastergrams from control *5HT3aR.Cre, NR1^{fl/fl}* (left) and *5HT3aR.Cre, NR1^{fl/fl}, GCaMP6s* (right) mice at P6.

(K) Percentages of correlated pairs in control ($n = 7$ movies, 4 mice) and *5HT3aR.Cre, NR1^{fl/fl}, GCaMP6s* ($n = 10$ movies, 4 mice) mice. Unpaired t test, $p < 0.0001$.

(L) Active cells in network events. Unpaired t test, $p = 0.039$.

(M) Quantification of event frequency. Unpaired t test, $p = 0.27$.

(N) Quantification of event duration. Unpaired t test, $p = 0.25$. ns, $p > 0.05$. * $p < 0.05$, **** $p < 0.0001$, Error bars indicate SEM. See also Figure S7 and Table S4.



(legend on next page)

powerful inhibitory effect on the spread of population activity in the neocortex (Kirmse et al., 2015; Minlebaev et al., 2007). Although the effects of GABA are complex and may vary within brain regions, cell compartment, and developmental stages (Fishell and Rudy, 2011; Oh et al., 2016), our observations support an inhibitory network function and provide mechanistic insight into the role of specific interneurons in the assembly of somatosensory circuits.

We show that activation of 5HT3aR Re interneurons in LI is necessary to refine the somatosensory receptive fields through an inhibitory effect gated by sensory inputs during the first postnatal week. This circuit mechanism provides an early source of inhibition that may operate before the functional maturation of parvalbumin-expressing interneurons, which occurs in the second through fourth postnatal weeks (Cruikshank et al., 2007; Okaty et al., 2009). In agreement with this notion, fewer Lhx6 interneurons participate in network events, and their activity is less correlated compared to that of the 5HT3aR population at P6 (Figures 1F and 1G). In addition, previous studies revealed that efferent connections from deep layer somatostatin-expressing interneurons to superficial layers are also weak in the first postnatal week (Anastasiades et al., 2016).

Previous evidence indicates that spindle bursts are the most prominent pattern of network activity in the somatosensory cortex during the first postnatal week. These patterns can be generated by intrinsic cortical oscillations as well as by rhythmic inputs initiated in thalamic neurons (Minlebaev et al., 2011; Yang et al., 2013). While sensory- and thalamic-evoked inputs trigger activity in whisker-related cortical columns, spontaneous calcium events in layer II/III form neuronal microdomains that are not contained within barrel boundaries (Golshani et al., 2009; Yuste et al., 1992). Moreover, the synchronization within these spontaneous microdomains is not affected by sensory deprivation, suggesting that they are generated by an intrinsic mechanism (Golshani et al., 2009). Based on our data, we propose a model in which 5HT3aR Re interneurons, activated by thalamic inputs, suppress spontaneous microdomains and promote the formation of barrel columns tuned to individual whiskers. The local inhibitory role of 5HT3aR Re interneurons is crucial, since

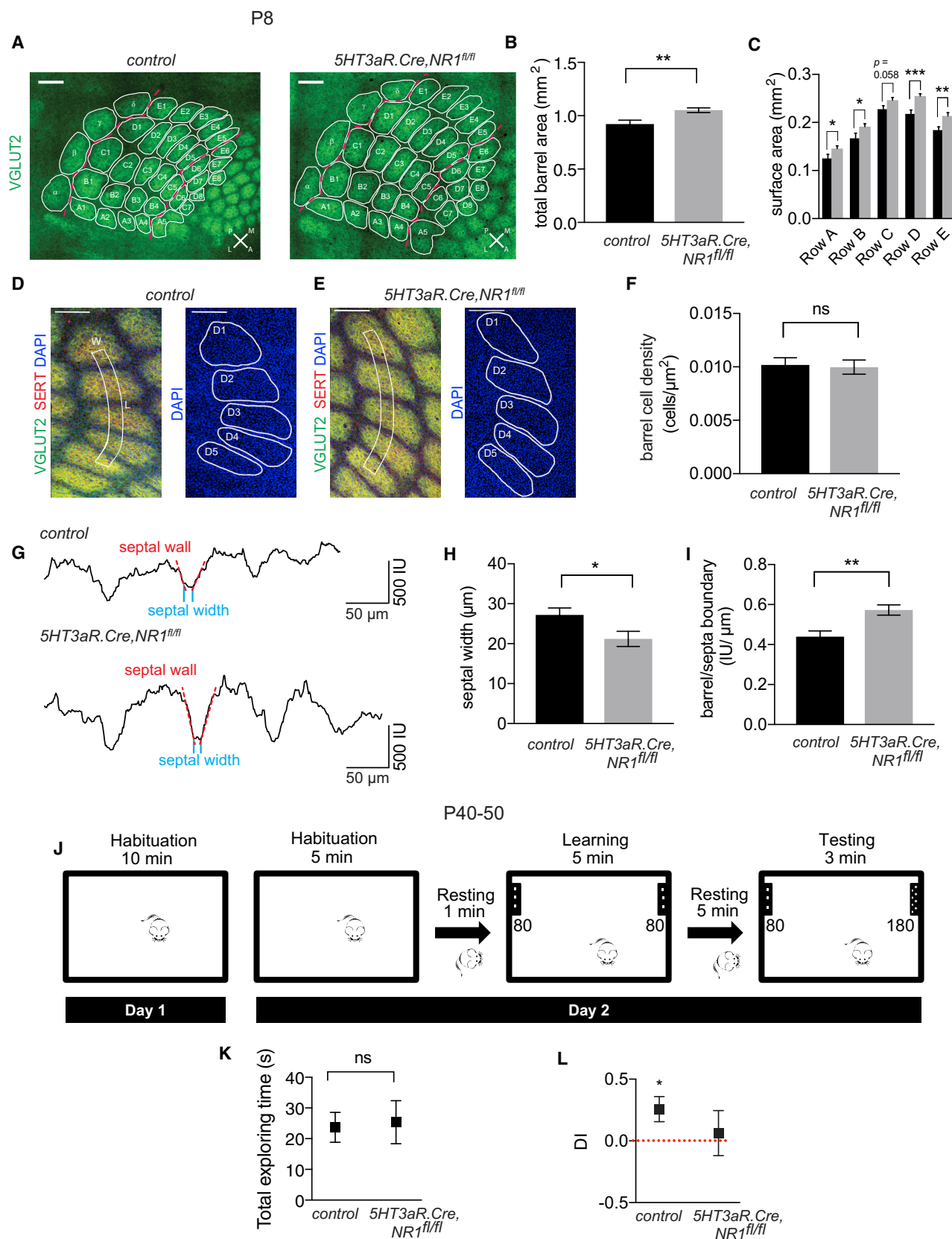
their recruitment occurs at a developmental stage when connectivity from deep to superficial layers has yet to mature (Stern et al., 2001).

How does early developmental impairment of 5HT3aR Re interneurons affect the long-term organization of the somatosensory system? Columnar refinement of LIV-LII/III connections begins at the end of the first postnatal week, and sensory deprivation weakens this connection through long-term depression (Bender et al., 2006; Shepherd et al., 2003). Therefore, reduced inhibition at P6 could affect columnar refinement and thus weaken LIV-LII/III connections. Indeed, we show that fewer pyramidal cells responded to whisker stimulation in *5HT3aR.Cre, NR1^{fl/fl}* mice at P12 (Figures S8G–S8I). In addition, we found that NMDAR knockdown leads to an impairment in somatosensory performance in adult mice. Although NMDAR removal in our experiments is not restricted to developing 5HT3aR Re interneurons within the somatosensory cortex, we provide several pieces of complementary evidence that point to a somatosensory defect, including a loss of thalamic inputs from the VPM, barrel enlargement, and functional expansion of pyramidal cell responses at neonatal stages. In addition, no significant differences in exploratory activity or overt motor defects are observed in *5HT3aR.Cre, NR1^{fl/fl}* compared to control mice. These behaviors involve the amygdala and motor nuclei (Bailey and Crawley, 2009) areas, which also contain 5HT3aR Re interneurons (Allen Developing Mouse Brain Atlas, 2008; Nery et al., 2002). Altogether, these data indicate that behavioral defects are likely a consequence of impaired maturation of somatosensory circuits. Our results complement recent findings indicating that other neuronal types may contribute to the maturation of deep layer circuits at neonatal stages (Marques-Smith et al., 2016; Tuncdemir et al., 2016) and provide a circuit mechanism for inhibition in superficial cortical layers. More generally, these findings indicate that the maturation of inhibitory networks in response to early experience may be a general rule in the development of sensory maps (Quast et al., 2017; Takesian et al., 2018).

In summary, our results indicate that the recruitment of select interneuron cell types by early experience is fundamental for the formation of topographic sensory maps that underlie mature brain function. Elevated network synchrony during critical

Figure 7. Increased Activation of Pyramidal Cells after NR1 Knockdown in 5HT3aR Re Interneurons

- (A) Representative Emx1-expressing starter cells (yellow) and presynaptic partners (red) in the somatosensory cortex at P8. Mice were injected with rabies at P1. Scale bar, 100 μ m.
- (B) Percentages of LI inputs to LII pyramidal cells over all cortical inputs (excitatory neurons and interneurons, $9.0\% \pm 2.7\%$) and all cortical interneuronal inputs ($13.5\% \pm 5.4\%$, $n = 2$ mice).
- (C) Schematics for optogenetic probing of LII pyramidal neurons after stimulation of LI 5HT3aR Re interneurons. ChR2-expressing 5HT3aR neurons were stimulated with LED 488 light in LI only. PC, pyramidal cell.
- (D) Representative average IPSC recorded from a LII PC upon light stimulation before (black) and after TTX and 4-AP (red) application for monosynaptic responses.
- (E) Schematic representation for the imaging of LII/III PCs.
- (F) Schematic representation of targeted GCaMP6s expression in PCs.
- (G) Representative event histograms and rastergrams for control *NR1^{fl/fl}* (top) and *5HT3aR.Cre, NR1^{fl/fl}* (bottom) mice. Red vertical lines mark the onsets of whisker stimulation (WS) by air puff and vertical red shaded areas depict the time windows (5 s) during which network events were quantified. Blue horizontal lines indicate the threshold for network events. Each line in the rastergram represents a calcium event from onset to offset.
- (H) Number of network events after whisker stimulation in 9-min movies in control ($n = 5$ movies, 3 mice) and *5HT3aR.Cre, NR1^{fl/fl}* ($n = 7$ movies, 3 mice) mice. Mann-Whitney test, $p = 0.02$.
- (I) Percentage of activated neurons during network events. Mann-Whitney test, $p = 0.01$.
- (J) Plot of average correlation coefficients as a function of distance between all cell pairs. Datasets were fitted with exponential decay. Extra-sum-of-squares F test, $p < 0.0001$ (different curves for each dataset). * $p < 0.05$, **** $p < 0.0001$. Error bars indicate SEM. See also Figures S7 and S8.



(legend on next page)

periods for experience-dependent circuit development is observed in mouse models of neurodevelopmental disorders (Gonçalves et al., 2013) and may underlie the cognitive and sensory deficits observed in patients (Marín, 2012). As such, results from this study may be particularly relevant for our understanding of cell-type-specific network dysfunctions in these disorders.

STAR★METHODS

Detailed methods are provided in the online version of this paper and include the following:

- KEY RESOURCES TABLE
- CONTACT FOR REAGENT AND RESOURCE SHARING
- EXPERIMENTAL MODEL AND SUBJECT DETAILS
- METHOD DETAILS
 - Viral Injections
 - *In Utero* Electroporations
 - Rabies Viral Tracing
 - Immunohistochemistry
 - Barrel Field Analysis
 - Cranial Window Surgery
 - *In Vivo* Two-Photon Calcium Imaging
 - Whisker Stimulation
 - Imaging Data Processing and Transient Detection
 - Imaging Data Analysis
 - Sensory Deprivation
 - Electrophysiology
 - Tactile Discrimination Task
- QUANTIFICATION AND STATISTICAL ANALYSIS

SUPPLEMENTAL INFORMATION

Supplemental Information includes eight figures, four tables, and two videos and can be found with this article online at <https://doi.org/10.1016/j.neuron.2018.06.002>.

A video abstract is available at <https://doi.org/10.1016/j.neuron.2018.06.002#mmc5>.

ACKNOWLEDGMENTS

We are grateful to Z. Duan, P. Chu, J. Kaltschmidt, J. Ackman, D. Pisapia, and T. Ryan for comments on the manuscript. We thank J. Witzum for help with the whisker stimulation and imaging setup, W. Gan and B. Rudy for helpful discussions, and T. Otsuka and S. Baksh for technical assistance. In addition, we recognize the generosity of the Genetically-Encoded Neuronal Indicator and Effector (GENIE) Project and the Janelia Research Campus for making GCaMP6s available. This work was supported by grants from NIH (NIMH 1R01MH110553-01), Pediatric Epilepsies Award (Citizens United for Research in Epilepsy), Leon Levy Fellowship Award (Leon Levy Foundation), and Frueauff Foundation Award to N.V.D.M.G.; NIMH (1R01 MH109685) to C.L.; and NIGMS (T32GM007739) to Weill Cornell/Rockefeller/Sloan Kettering Tri-Institutional MD-PhD Program in support for R.B., A.F.I., and R.N.F.

AUTHOR CONTRIBUTIONS

A.C. and N.V.D.M.G. designed the research. A.C. performed and analyzed electrophysiological recordings, neuronal morphology, immunohistochemistry, and calcium imaging experiments. R.B. performed rabies viral tracing, morphological analysis, immunohistochemistry, and a subset of calcium imaging experiments. A.F.I. and M.F. performed the analysis of barrel anatomy. R.N.F. and C.L. designed the behavioral task in collaboration with A.C. and provided assistance with calcium imaging analysis. R.N.F. performed and analyzed the behavioral experiments. G.F. provided mouse and viral strains. N.V.D.M.G. supervised the research and secured funding. A.C. and N.V.D.M.G. wrote the manuscript with the help of all authors.

DECLARATION OF INTERESTS

The authors declare no competing interests.

Received: December 5, 2017

Revised: April 26, 2018

Accepted: June 1, 2018

Published: June 21, 2018

REFERENCES

Ackman, J.B., Burbridge, T.J., and Crair, M.C. (2012). Retinal waves coordinate patterned activity throughout the developing visual system. *Nature* 490, 219–225.

Figure 8. Increased Barrel Size and Impaired Texture Discrimination after NR1 Knockdown in 5HT3aR Re Interneurons

- (A) Representative images of barrel fields in control *NR1^{fl/fl}* and *5HT3aR.Cre, NR1^{fl/fl}* mice at P8. Thalamic afferents were visualized by VGLUT2 immunohistochemistry. Individual barrels are outlined in white. Red dotted lines indicate the boundaries within which barrels and septa were analyzed. Each of the 36 principal barrels was present in control and *5HT3aR.Cre, NR1^{fl/fl}* mice. A, anterior; P, posterior; M, medial; L, lateral. Scale bar, 200 μ m.
- (B) Quantification of total barrel area as the sum of the areas of individual barrels (A1–A4, B1–B4, C1–C5, D1–D5, E1–E5). Unpaired t test, $p = 0.0065$. Control: $n = 6$ mice; *5HT3aR.Cre, NR1^{fl/fl}*: $n = 9$ mice.
- (C) Quantification of barrel areas as the sum of individual barrel areas per row (row A to E). Multiple t tests comparing control and *5HT3aR.Cre, NR1^{fl/fl}*; row A: $p = 0.043$; row B: $p = 0.017$; row C: $p = 0.058$; row D: $p = 0.00035$; row E: $p = 0.0037$.
- (D) Representative images of row D in a control mouse at P8. Thalamic afferents were visualized by VGLUT2 and SERT immunohistochemistry (left). White outlines indicate areas used for quantification in (G)–(I) (left). D1 to D5 barrels are outlined on the same sections labeled with DAPI (right). Scale bar, 100 μ m.
- (E) Representative images of D row in a *5HT3aR.Cre, NR1^{fl/fl}* mouse at P8. Scale bar, 100 μ m.
- (F) Average cell density in D barrels quantified as the sum of DAPI-labeled cells in all D barrels divided by the total surface area. Unpaired t test, $p = 0.84$. control: $n = 3$ mice, *5HT3aR.Cre, NR1^{fl/fl}*: $n = 3$ mice.
- (G) Fluorescence intensity traces across D1 to D5 barrel centers in control (top) and *5HT3aR.Cre, NR1^{fl/fl}* (bottom). Red dotted lines indicate barrel/septa boundary measured as the septal slope.
- (H) Average septal width in D row. Unpaired t test, $p = 0.046$. Control: $n = 6$ mice, *5HT3aR.Cre, NR1^{fl/fl}*: $n = 9$ mice.
- (I) Average barrel/septa boundary. Unpaired t test, $p = 0.0046$.
- (J) Schematic diagrams for tactile discrimination test. The sheets of sandpaper used were 80- and 180-grit.
- (K) Quantification of total time spent exploring both sheets. Unpaired t test, $p = 0.84$. *NR1^{fl/fl}* control: $n = 14$ mice, *5HT3aR.Cre, NR1^{fl/fl}*: $n = 8$ mice.
- (L) Discrimination index (DI = time spent with 180-grit/total time spent exploring). DI was significantly different from chance level in control, but not mutant, mice (DI = 0.5, red dotted line). One-sample t test, control: $p = 0.02$, *5HT3aR.Cre, NR1^{fl/fl}*: $p = 0.74$. ns: $p > 0.05$, * $p < 0.05$, ** $p < 0.01$, *** $p < 0.001$. Error bars indicate SEM.

- Agmon, A., and Connors, B.W. (1991). Thalamocortical responses of mouse somatosensory (barrel) cortex in vitro. *Neuroscience* 41, 365–379.
- Akhmetshina, D., Nasretidinov, A., Zakharov, A., Valeeva, G., and Khazipov, R. (2016). The nature of the sensory input to the neonatal rat barrel cortex. *J. Neurosci.* 36, 9922–9932.
- Allen Developing Mouse Brain Atlas (2008). Available from: developingmouse.brain-map.org.
- Allène, C., Cattani, A., Ackman, J.B., Bonifazi, P., Aniksztejn, L., Ben-Ari, Y., and Cossart, R. (2008). Sequential generation of two distinct synapse-driven network patterns in developing neocortex. *J. Neurosci.* 28, 12851–12863.
- Anastasiades, P.G., Marques-Smith, A., Lyngholm, D., Lickiss, T., Raffiq, S., Kätzel, D., Miesenböck, G., and Butt, S.J.B. (2016). GABAergic interneurons form transient layer-specific circuits in early postnatal neocortex. *Nat. Commun.* 7, 10584.
- Ascoli, G.A., Alonso-Nanclares, L., Anderson, S.A., Barrionuevo, G., Benavides-Picione, R., Burkhalter, A., Buzsáki, G., Cauli, B., Defelipe, J., Fairén, A., et al.; Petilla Interneuron Nomenclature Group (2008). Petilla terminology: nomenclature of features of GABAergic interneurons of the cerebral cortex. *Nat. Rev. Neurosci.* 9, 557–568.
- Bailey, K.R., and Crawley, J.N. (2009). Anxiety-related behaviors in mice. In *Methods of Behavior Analysis in Neuroscience*, Chapter 5, Second Edition, J.J. Buccafusco, ed. (CRC Press/Taylor & Francis).
- Batista-Brito, R., and Fishell, G. (2009). The developmental integration of cortical interneurons into a functional network. In *Development of Neural Circuitry* 87, Chapter 3, O. Hobert, ed. (Elsevier), pp. 81–118.
- Batista-Brito, R., Vinck, M., Ferguson, K.A., Chang, J.T., Laubender, D., Lur, G., Mossner, J.M., Hernandez, V.G., Ramakrishnan, C., Deisseroth, K., et al. (2017). Developmental dysfunction of VIP interneurons impairs cortical circuits. *Neuron* 95, 884–895.e9.
- Ben-Ari, Y. (2002). Excitatory actions of gaba during development: the nature of the nurture. *Nat. Rev. Neurosci.* 3, 728–739.
- Bender, K.J., Allen, C.B., Bender, V.A., and Feldman, D.E. (2006). Synaptic basis for whisker deprivation-induced synaptic depression in rat somatosensory cortex. *J. Neurosci.* 26, 4155–4165.
- Burbridge, T.J., Xu, H.-P., Ackman, J.B., Ge, X., Zhang, Y., Ye, M.-J., Zhou, Z.-J., Xu, J., Contractor, A., and Crair, M.C. (2014). Visual circuit development requires patterned activity mediated by retinal acetylcholine receptors. *Neuron* 84, 1049–1064.
- Cardin, J.A., Carlén, M., Meletis, K., Knoblich, U., Zhang, F., Deisseroth, K., Tsai, L.-H., and Moore, C.I. (2009). Driving fast-spiking cells induces gamma rhythm and controls sensory responses. *Nature* 459, 663–667.
- Che, A., Truong, D.T., Fitch, R.H., and LoTurco, J.J. (2016). Mutation of the dyslexia-associated gene *Dcdc2* enhances glutamatergic synaptic transmission between layer 4 neurons in mouse neocortex. *Cereb. Cortex* 26, 3705–3718.
- Chen, J., and Kriegstein, A.R. (2015). A GABAergic projection from the zona incerta to cortex promotes cortical neuron development. *Science* 350, 554–558.
- Chen, T.W., Wardill, T.J., Sun, Y., Pulver, S.R., Renninger, S.L., Baohan, A., Schreier, E.R., Kerr, R.A., Orger, M.B., Jayaraman, V., et al. (2013). Ultrasensitive fluorescent proteins for imaging neuronal activity. *Nature* 499, 295–300.
- Chen, C.C., Lu, J., Yang, R., Ding, J.B., and Zuo, Y. (2017). Selective activation of parvalbumin interneurons prevents stress-induced synapse loss and perceptual defects. *Mol. Psychiatry*. Published online August 1, 2017. <https://doi.org/10.1038/mp.2017.159>.
- Chittajallu, R., and Isaac, J.T.R. (2010). Emergence of cortical inhibition by coordinated sensory-driven plasticity at distinct synaptic loci. *Nat. Neurosci.* 13, 1240–1248.
- Chittajallu, R., Wester, J.C., Craig, M.T., Barksdale, E., Yuan, X.Q., Akgül, G., Fang, C., Collins, D., Hunt, S., Pelkey, K.A., and McBain, C.J. (2017). Afferent specific role of NMDA receptors for the circuit integration of hippocampal neurogliaform cells. *Nat. Commun.* 8, 152.
- Chiu, C., and Weliky, M. (2001). Spontaneous activity in developing ferret visual cortex in vivo. *J. Neurosci.* 21, 8906–8914.
- Chowdhury, T.G., Jimenez, J.C., Bomar, J.M., Cruz-Martin, A., Cantle, J.P., and Portera-Cailliau, C. (2010). Fate of cajal-retzius neurons in the postnatal mouse neocortex. *Front. Neuroanat.* 4, 10.
- Clancy, K.B., Schnepel, P., Rao, A.T., and Feldman, D.E. (2015). Structure of a single whisker representation in layer 2 of mouse somatosensory cortex. *J. Neurosci.* 35, 3946–3958.
- Crépel, V., Aronov, D., Jorquera, I., Represa, A., Ben-Ari, Y., and Cossart, R. (2007). A parturition-associated nonsynaptic coherent activity pattern in the developing hippocampus. *Neuron* 54, 105–120.
- Cruikshank, S.J., Lewis, T.J., and Connors, B.W. (2007). Synaptic basis for intense thalamocortical activation of feedforward inhibitory cells in neocortex. *Nat. Neurosci.* 10, 462–468.
- Cruikshank, S.J., Ahmed, O.J., Stevens, T.R., Patrick, S.L., Gonzalez, A.N., Elmaleh, M., and Connors, B.W. (2012). Thalamic control of layer 1 circuits in prefrontal cortex. *J. Neurosci.* 32, 17813–17823.
- De Marco García, N.V., and Fishell, G. (2014). Subtype-selective electroporation of cortical interneurons. *J. Vis. Exp.* Published online August 18, 2014. <https://doi.org/10.3791/51518>.
- De Marco García, N.V., Karayannis, T., and Fishell, G. (2011). Neuronal activity is required for the development of specific cortical interneuron subtypes. *Nature* 472, 351–355.
- De Marco García, N.V., Priya, R., Tuncdemir, S.N., Fishell, G., and Karayannis, T. (2015). Sensory inputs control the integration of neurogliaform interneurons into cortical circuits. *Nat. Neurosci.* 18, 393–401.
- Dombeck, D.A., Khabbazi, A.N., Collman, F., Adelman, T.L., and Tank, D.W. (2007). Imaging large-scale neural activity with cellular resolution in awake, mobile mice. *Neuron* 56, 43–57.
- Egorov, A.V., and Draguhn, A. (2013). Development of coherent neuronal activity patterns in mammalian cortical networks: common principles and local heterogeneity. *Mech. Dev.* 130, 412–423.
- Fishell, G., and Rudy, B. (2011). Mechanisms of inhibition within the telencephalon: “where the wild things are”. *Annu. Rev. Neurosci.* 34, 535–567.
- Fox, K. (1995). The critical period for long-term potentiation in primary sensory cortex. *Neuron* 15, 485–488.
- Garaschuk, O., Linn, J., Eilers, J., and Konnerth, A. (2000). Large-scale oscillatory calcium waves in the immature cortex. *Nat. Neurosci.* 3, 452–459.
- Golshani, P., Gonçalves, J.T., Khoshkhou, S., Mostany, R., Smirnakis, S., and Portera-Cailliau, C. (2009). Internally mediated developmental desynchronization of neocortical network activity. *J. Neurosci.* 29, 10890–10899.
- Gonçalves, J.T., Anstey, J.E., Golshani, P., and Portera-Cailliau, C. (2013). Circuit level defects in the developing neocortex of fragile X mice. *Nat. Neurosci.* 16, 903–909.
- Gorski, J.A., Talley, T., Qiu, M., Puelles, L., Rubenstein, J.L.R., and Jones, K.R. (2002). Cortical excitatory neurons and glia, but not GABAergic neurons, are produced in the *Emx1*-expressing lineage. *J. Neurosci.* 22, 6309–6314.
- Haubensak, W., Kunwar, P.S., Cai, H., Ciocchi, S., Wall, N.R., Ponnusamy, R., Biag, J., Dong, H.-W., Deisseroth, K., Callaway, E.M., et al. (2010). Genetic dissection of an amygdala microcircuit that gates conditioned fear. *Nature* 468, 270–276.
- He, C.X., Cantu, D.A., Mantri, S.S., Zeiger, W.A., Goel, A., and Portera-Cailliau, C. (2017). Tactile defensiveness and impaired adaptation of neuronal activity in the *Fmr1* knock-out mouse model of autism. *J. Neurosci.* 37, 6475–6487.
- Inta, D., Alfonso, J., von Engelhardt, J., Kreuzberg, M.M., Meyer, A.H., van Hooff, J.A., and Monyer, H. (2008). Neurogenesis and widespread forebrain migration of distinct GABAergic neurons from the postnatal subventricular zone. *Proc. Natl. Acad. Sci. USA* 105, 20994–20999.
- Isaacson, J.S., and Scanziani, M. (2011). How inhibition shapes cortical activity. *Neuron* 72, 231–243.
- Jiang, X., Wang, G., Lee, A.J., Stornetta, R.L., and Zhu, J.J. (2013). The organization of two new cortical interneuronal circuits. *Nat. Neurosci.* 16, 210–218.

- Jiang, X., Shen, S., Cadwell, C.R., Berens, P., Sinz, F., Ecker, A.S., Patel, S., and Tolias, A.S. (2015). Principles of connectivity among morphologically defined cell types in adult neocortex. *Science* 350, aac9462.
- Kanold, P.O., and Shatz, C.J. (2006). Subplate neurons regulate maturation of cortical inhibition and outcome of ocular dominance plasticity. *Neuron* 51, 627–638.
- Karnani, M.M., Jackson, J., Ayzenshtat, I., Tucciarone, J., Manoocher, K., Snider, W.G., and Yuste, R. (2016). Cooperative subnetworks of molecularly similar interneurons in mouse neocortex. *Neuron* 90, 86–100.
- Khazipov, R., Sirota, A., Leinekugel, X., Holmes, G.L., Ben-Ari, Y., and Buzsáki, G. (2004). Early motor activity drives spindle bursts in the developing somatosensory cortex. *Nature* 432, 758–761.
- Kirkby, L.A., Sack, G.S., Firl, A., and Feller, M.B. (2013). A role for correlated spontaneous activity in the assembly of neural circuits. *Neuron* 80, 1129–1144.
- Kirmse, K., Kummer, M., Kovalchuk, Y., Witte, O.W., Garaschuk, O., and Holthoff, K. (2015). GABA depolarizes immature neurons and inhibits network activity in the neonatal neocortex in vivo. *Nat. Commun.* 6, 7750.
- Kwan, A.C., and Dan, Y. (2012). Dissection of cortical microcircuits by single-neuron stimulation *in vivo*. *Curr. Biol.* 22, 1459–1467.
- Lee, S., Hjerling-Leffler, J., Zagha, E., Fishell, G., and Rudy, B. (2010). The largest group of superficial neocortical GABAergic interneurons expresses ionotropic serotonin receptors. *J. Neurosci.* 30, 16796–16808.
- Lee, S., Kruglikov, I., Huang, Z.J., Fishell, G., and Rudy, B. (2013). A disinhibitory circuit mediates motor integration in the somatosensory cortex. *Nat. Neurosci.* 16, 1662–1670.
- Lee, A.J., Wang, G., Jiang, X., Johnson, S.M., Hoang, E.T., Lanté, F., Stornetta, R.L., Beenhakker, M.P., Shen, Y., and Julius Zhu, J. (2015). Canonical organization of layer 1 neuron-led cortical inhibitory and disinhibitory interneuronal circuits. *Cereb. Cortex* 25, 2114–2126.
- Leighton, A.H., and Lohmann, C. (2016). The wiring of developing sensory circuits—from patterned spontaneous activity to synaptic plasticity mechanisms. *Front. Neural Circuits* 10, 71.
- Louvi, A., Yoshida, M., and Grove, E.A. (2007). The derivatives of the Wnt3a lineage in the central nervous system. *J. Comp. Neurol.* 504, 550–569.
- Marín, O. (2012). Interneuron dysfunction in psychiatric disorders. *Nat. Rev. Neurosci.* 13, 107–120.
- Marín, O., Anderson, S.A., and Rubenstein, J.L.R. (2000). Origin and molecular specification of striatal interneurons. *J. Neurosci.* 20, 6063–6076.
- Markram, H., Toledo-Rodriguez, M., Wang, Y., Gupta, A., Silberberg, G., and Wu, C. (2004). Interneurons of the neocortical inhibitory system. *Nat. Rev. Neurosci.* 5, 793–807.
- Marques-Smith, A., Lyngholm, D., Kaufmann, A.-K., Stacey, J.A., Hoerder-Suabedissen, A., Becker, E.B.E., Wilson, M.C., Molnár, Z., and Butt, S.J.B. (2016). A transient transaminar GABAergic interneuron circuit connects thalamocortical recipient layers in neonatal somatosensory cortex. *Neuron* 89, 536–549.
- Miceli, S., Negwer, M., van Eijs, F., Kalkhoven, C., van Lierop, I., Homberg, J., and Schubert, D. (2013). High serotonin levels during brain development alter the structural input-output connectivity of neural networks in the rat somatosensory layer IV. *Front. Cell. Neurosci.* 7, 88.
- Minlebaev, M., Ben-Ari, Y., and Khazipov, R. (2007). Network mechanisms of spindle-burst oscillations in the neonatal rat barrel cortex in vivo. *J. Neurophysiol.* 97, 692–700.
- Minlebaev, M., Colonnese, M., Tsintsadze, T., Sirota, A., and Khazipov, R. (2011). Early γ oscillations synchronize developing thalamus and cortex. *Science* 334, 226–229.
- Moody, W.J., and Bosma, M.M. (2005). Ion channel development, spontaneous activity, and activity-dependent development in nerve and muscle cells. *Physiol. Rev.* 85, 883–941.
- Muñoz, W., Tremblay, R., Levenstein, D., and Rudy, B. (2017). Layer-specific modulation of neocortical dendritic inhibition during active wakefulness. *Science* 355, 954–959.
- Narbout-Nême, N., Pavone, L.M., Avallone, L., Zhuang, X., and Gaspar, P. (2008). Serotonin transporter transgenic (SERT^{cr6}) mouse line reveals developmental targets of serotonin specific reuptake inhibitors (SSRIs). *Neuropharmacology* 55, 994–1005.
- Nery, S., Fishell, G., and Corbin, J.G. (2002). The caudal ganglionic eminence is a source of distinct cortical and subcortical cell populations. *Nat. Neurosci.* 5, 1279–1287.
- Oh, W.C., Lutz, S., Castillo, P.E., and Kwon, H.-B. (2016). De novo synaptogenesis induced by GABA in the developing mouse cortex. *Science* 353, 1037–1040.
- Okaty, B.W., Miller, M.N., Sugino, K., Hempel, C.M., and Nelson, S.B. (2009). Transcriptional and electrophysiological maturation of neocortical fast-spiking GABAergic interneurons. *J. Neurosci.* 29, 7040–7052.
- Oláh, S., Komlósi, G., Szabadics, J., Varga, C., Tóth, E., Barzó, P., and Tamás, G. (2007). Output of neurogliaform cells to various neuron types in the human and rat cerebral cortex. *Front. Neural Circuits* 1, 4.
- Overstreet-Wadiche, L., and McBain, C.J. (2015). Neurogliaform cells in cortical circuits. *Nat. Rev. Neurosci.* 16, 458–468.
- Peron, S.P., Freeman, J., Iyer, V., Guo, C., and Svoboda, K. (2015). A cellular resolution map of barrel cortex activity during tactile behavior. *Neuron* 86, 783–799.
- Petersen, C.C.H. (2007). The functional organization of the barrel cortex. *Neuron* 56, 339–355.
- Pinto, L., and Dan, Y. (2015). Cell-type-specific activity in prefrontal cortex during goal-directed behavior. *Neuron* 87, 437–450.
- Porter, J.T., Johnson, C.K., and Agmon, A. (2001). Diverse types of interneurons generate thalamus-evoked feedforward inhibition in the mouse barrel cortex. *J. Neurosci.* 21, 2699–2710.
- Pouchelon, G., Gambino, F., Bellone, C., Telley, L., Vitali, I., Lüscher, C., Holtmaat, A., and Jabaudon, D. (2014). Modality-specific thalamocortical inputs instruct the identity of postsynaptic L4 neurons. *Nature* 511, 471–474.
- Quast, K.B., Ung, K., Froudarakis, E., Huang, L., Herman, I., Addison, A.P., Ortiz-Guzman, J., Cordiner, K., Saggau, P., Tolias, A.S., and Arenkiel, B.R. (2017). Developmental broadening of inhibitory sensory maps. *Nat. Neurosci.* 20, 189–199.
- Rajasethupathy, P., Sankaran, S., Marshel, J.H., Kim, C.K., Ferenczi, E., Lee, S.Y., Berndt, A., Ramakrishnan, C., Jaffe, A., Lo, M., et al. (2015). Projections from neocortex mediate top-down control of memory retrieval. *Nature* 526, 653–659.
- Rocheffort, N.L., Garaschuk, O., Milos, R.-I., Narushima, M., Marandi, N., Pichler, B., Kovalchuk, Y., and Konnerth, A. (2009). Sparsification of neuronal activity in the visual cortex at eye-opening. *Proc. Natl. Acad. Sci. USA* 106, 15049–15054.
- Schwartz, T.H., Rabinowitz, D., Unni, V., Kumar, V.S., Smetters, D.K., Tsiola, A., and Yuste, R. (1998). Networks of coactive neurons in developing layer 1. *Neuron* 20, 541–552.
- Shen, J., and Colonnese, M.T. (2016). Development of activity in the mouse visual cortex. *J. Neurosci.* 36, 12259–12275.
- Shepherd, G.M.G., Pologruto, T.A., and Svoboda, K. (2003). Circuit analysis of experience-dependent plasticity in the developing rat barrel cortex. *Neuron* 38, 277–289.
- Siegel, F., Heimel, J.A., Peters, J., and Lohmann, C. (2012). Peripheral and central inputs shape network dynamics in the developing visual cortex in vivo. *Curr. Biol.* 22, 253–258.
- Staiger, J.F., Bojak, I., Miceli, S., and Schubert, D. (2015). A gradual depth-dependent change in connectivity features of supragranular pyramidal cells in rat barrel cortex. *Brain Struct. Funct.* 220, 1317–1337.
- Steinmetz, N.A., Buettner, C., Lecoq, J., Lee, C.R., Peters, A.J., Jacobs, E.A.K., Coen, P., Ollerenshaw, D.R., Valley, M.T., de Vries, S.E.J., et al. (2017). Aberrant cortical activity in multiple GCaMP6-expressing transgenic mouse lines. *eNeuro* 4, ENEURO.0207-17.2017.

- Stern, E.A., Maravall, M., and Svoboda, K. (2001). Rapid development and plasticity of layer 2/3 maps in rat barrel cortex in vivo. *Neuron* 31, 305–315.
- Stirman, J.N., Smith, I.T., Kudenov, M.W., and Smith, S.L. (2016). Wide field-of-view, multi-region, two-photon imaging of neuronal activity in the mammalian brain. *Nat. Biotechnol.* 34, 857–862.
- Takesian, A.E., Bogart, L.J., Lichtman, J.W., and Hensch, T.K. (2018). Inhibitory circuit gating of auditory critical-period plasticity. *Nat. Neurosci.* 21, 218–227.
- Taniguchi, H., He, M., Wu, P., Kim, S., Paik, R., Sugino, K., Kvitsiani, D., Fu, Y., Lu, J., Lin, Y., et al. (2011). A resource of Cre driver lines for genetic targeting of GABAergic neurons in cerebral cortex. *Neuron* 71, 995–1013.
- Tolner, E.A., Sheikh, A., Yukin, A.Y., Kaila, K., and Kanold, P.O. (2012). Subplate neurons promote spindle bursts and thalamocortical patterning in the neonatal rat somatosensory cortex. *J. Neurosci.* 32, 692–702.
- Tremblay, R., Lee, S., and Rudy, B. (2016). GABAergic interneurons in the neocortex: from cellular properties to circuits. *Neuron* 91, 260–292.
- Tuncdemir, S.N., Wamsley, B., Stam, F.J., Osakada, F., Goulding, M., Callaway, E.M., Rudy, B., and Fishell, G. (2016). Early somatostatin interneuron connectivity mediates the maturation of deep layer cortical circuits. *Neuron* 89, 521–535.
- Valeeva, G., Tressard, T., Mukhtarov, M., Baude, A., and Khazipov, R. (2016). An optogenetic approach for investigation of excitatory and inhibitory network GABA actions in mice expressing channelrhodopsin-2 in GABAergic neurons. *J. Neurosci.* 36, 5961–5973.
- Woolsey, T.A., and Van der Loos, H. (1970). The structural organization of layer IV in the somatosensory region (SI) of mouse cerebral cortex. The description of a cortical field composed of discrete cytoarchitectonic units. *Brain Res.* 17, 205–242.
- Woolsey, T.A., and Wann, J.R. (1976). Areal changes in mouse cortical barrels following vibrissal damage at different postnatal ages. *J. Comp. Neurol.* 170, 53–66.
- Wozny, C., and Williams, S.R. (2011). Specificity of synaptic connectivity between layer 1 inhibitory interneurons and layer 2/3 pyramidal neurons in the rat neocortex. *Cereb. Cortex* 21, 1818–1826.
- Wu, H.-P.P., Ioffe, J.C., Iverson, M.M., Boon, J.M., and Dyck, R.H. (2013). Novel, whisker-dependent texture discrimination task for mice. *Behav. Brain Res.* 237, 238–242.
- Yang, J.W., An, S., Sun, J.J., Reyes-Puerta, V., Kindler, J., Berger, T., Kilb, W., and Luhmann, H.J. (2013). Thalamic network oscillations synchronize ontogenetic columns in the newborn rat barrel cortex. *Cereb. Cortex* 23, 1299–1316.
- Yao, X.H., Wang, M., He, X.-N., He, F., Zhang, S.-Q., Lu, W., Qiu, Z.-L., and Yu, Y.-C. (2016). Electrical coupling regulates layer 1 interneuron microcircuit formation in the neocortex. *Nat. Commun.* 7, 12229.
- Yuste, R., Peinado, A., and Katz, L.C. (1992). Neuronal domains in developing neocortex. *Science* 257, 665–669.

STAR★METHODS

KEY RESOURCES TABLE

REAGENT or RESOURCES	SOURCE	IDENTIFIER
Antibodies		
Goat polyclonal anti-GFP	VRW	Cat No:600-101-215; RRID: AB_218182
Rat polyclonal anti-GFP	Nacalai USA	GF090R; RRID: AB_10013361
Chicken polyclonal anti-RFP	VRW	600-901-379; RRID: AB_10704808
Mouse monoclonal anti-Reelin	MBL	D223-3; RRID: AB_843523
Rabbit polyclonal anti-VIP	Immunostar	20077; RRID: AB_10730725
Guinea pig anti-VGluT2	EMD Millipore	AB2251; RRID: AB_2665454
Streptavidin-488	Thermo Fisher Scientific	S11223; RRID: AB_2336881
Streptavidin-Pacific Blue	Thermo Fisher Scientific	S11222
Rabbit anti-5HTT	Immunostar	24330; RRID: AB_10718084
Rabbit anti-Satb2	Abcam	ab34735; RRID: AB_2301417
Bacterial and Virus Strains		
<i>AAV1.syn.GCaMP6s.WPRE.SV40</i>	UPenn viral core	AV-1-PV2824
SADΔG mCherry (EnVA)	Made in house	N/A
<i>AAV1.EF1a.dflox.hChR2.mcherry.WPRE.hGH</i>	UPenn viral core	plasmid #37082
Chemicals, Peptides and Recombinant Proteins		
TTX	Abcam	ab120055
4-AP	Abcam	ab120003
SR-95531	Abcam	ab120042
NBQX	Abcam	ab120046
Experimental Models: Organisms/Strains		
Swiss Webster	Taconic	SW-F, SW-M
<i>VIP^{Cre}</i>	Jackson Laboratories	010908
<i>Lhx6^{Cre}</i>	Jackson Laboratories	026555
<i>Emx1^{Cre}</i>	Jackson Laboratories	005628
<i>SERT^{Cre}</i>	Jackson Laboratories	014554
<i>Wnt3a^{Cre}</i>	a gift from Ulrich Müller	N/A
<i>RCL-GCaMP6s</i> (Ai96)	Jackson Laboratories	024106
<i>RCL-ChR2</i> (Ai32)	Jackson Laboratories	024109
<i>NR1^{fl}</i>	Jackson Laboratories	005246
<i>5HT3aR^{Cre}</i>	a gift from N. Heintz, Rockefeller University	N/A
Recombinant DNA		
Dlx5/6-hGFP-TVA-B19G	De Marco García et al., 2015	N/A
pAAV-EF1a-FLEX-GTB	Callaway Lab; Haubensak et al., 2010	Addgene Plasmid #26197
Software and Algorithms		
CalciumDX	Ackman et al., 2012	https://github.com/ackman678/CalciumDX
Image Stabilizer	Kang, Li, "The Image Stabilizer plugin for Image J", February 2008. Copyright 2008–2009.	http://www.cs.cmu.edu/~kangli/code/Image_Stabilizer.html

CONTACT FOR REAGENT AND RESOURCE SHARING

Further information and requests for resources and reagents should be directed to and will be fulfilled by the Lead Contact, Natalia De Marco García (nad2018@med.cornell.edu).

EXPERIMENTAL MODEL AND SUBJECT DETAILS

Animal handling and experimentation were performed in accordance with US National Institute of Health and Weill Cornell Medical College Institutional Animal Care and Use Commission. Animals of both sexes were used and housed in a controlled environment on a 12 h light/dark cycle with food and water *ad libitum*. Swiss Webster (Taconic), *VIP^{Cre}* (Jackson Laboratories, 010908), *Lhx6.Cre* (Jackson Laboratories, 026555), *Emx1^{Cre}* (Jackson Laboratories, 005628), *SERT^{Cre}* (Jackson Laboratories, 014554), *Wnt3a^{Cre}* (a gift from Ulrich Müller), *RCL-GCaMP6s* (Ai96, Jackson Laboratories, 024106), *RCL-ChR2* (Ai32, Jackson Laboratories, 024109), *NR1^{fl}* (Jackson Laboratories, 005246), and *5HT3aR.Cre* (a gift from N. Heintz, Rockefeller University), were used for the studies. *5HT3aR.Cre*, *VIP^{Cre}*, *Lhx6.Cre*, *Emx1^{Cre}* and *Sert^{Cre}* were crossed with *RCL-GCaMP6s* (denoted as *5HT3aR.GCaMP6s*, *VIP.GCaMP6s*, *Lhx6.GCaMP6s*, *Emx1.GCaMP6s*, *Sert.GCaMP6s*). *5HT3aR.Cre* animals were crossed with *NR1^{fl/fl}* (denoted as *5HT3aR.Cre, NR1^{fl/fl}*). Information about mouse strains including genotyping protocols can be found at <https://www.jax.org/> and elsewhere (Gorski et al., 2002; Louvi et al., 2007; Narboux-Nême et al., 2008; Taniguchi et al., 2011).

METHOD DETAILS

Viral Injections

Stereotactic injections for calcium imaging or optogenetic stimulation were performed at P0. For rabies tracing experiments, stereotactic injections were performed at P0-P2 or P7-P9. *GCaMP6s* viral injections (AAV1.syn.*GCaMP6s.WPRE.SV40*, UPenn viral core) were performed on *5HT3aR.NR1^{fl/fl}* or *NR1^{fl/fl}* mice. ChR2 viral injections (AAV1.*Ef1a.DIO.hChR2.mCherry*, UPenn viral core) were performed on *SERT^{Cre}* or *SERT^{Cre}*, Ai32 mice. Modified rabies virus, *SADΔG* (SAD-deltaG_mCherry (EnvA)) was produced in the lab, was injected in electroporated mice for rabies tracing experiments (See *Rabies Viral Tracing* section for more information). Mice were anesthetized by hypothermia at P7 or younger stages, and isoflurane was used if they were older. Precise stereotactic coordinates and volume of virus injected in each animal were kept constant. In AAV.*GCaMP6s* imaging experiments, location of injections sites was confirmed by performing immunohistochemistry against GFP to reveal *GCaMP6s* expression after the imaging sessions. Glass micropipettes with a tip diameter of ~20 μm attached to a Nanoject (Drummond) injector were used for injections. For AAV viral injections, we injected 50 nL per animal.

In Utero Electroporations

In utero electroporation was performed as previously described (De Marco García et al., 2015, 2011). Briefly, pregnant mice were electroporated at embryonic day (E) E15.5 (De Marco García and Fishell, 2014). To target 5HT3aR Re populations, a *Dlx5/6-hGFP-TVA-B19G* plasmid (De Marco García et al., 2015) was electroporated into Swiss Webster mice. The *Distal-less 5/6* (*Dlx5/6*) enhancer element in this construct restricts expression of the *Histone2B.GFP* reporter, *TVA800* receptor and *B19G* glycoprotein to a small number of 5HT3aR Re interneurons (De Marco García et al., 2015). To target upper layer VIP-interneurons or *Emx1*-expressing excitatory neurons, an AAV-*EF1a-FLEX-GTB* plasmid (Addgene, Plasmid #26197) was electroporated into *VIP^{Cre}* or *Emx1^{Cre}* mice at E15.5. Animals were sacrificed 1 week after postnatal rabies injection: P7 for first postnatal week analyses and P14 for second postnatal week analyses.

Rabies Viral Tracing

Modified rabies viral injections on electroporated pups were carried out at either P0-P2 or P7-P9 using a Drummond Nanoject II (100 nL for Swiss Webster mice, 200 nL for *VIP^{Cre}* mice, and 2 nL for *Emx1^{Cre}* mice). Pups were then returned to the dam, and perfused for immunohistochemistry analysis 1 week later. Processing and analysis of rabies-infected brains were performed as previously described (De Marco García et al., 2015). In brief, consecutive 20 μm sections were collected on a cryostat (Leica CM3050S). Sections were immunostained for eGFP and RFP, and were examined under a Leica M165FC fluorescent microscope for double fluorescence to identify starter neurons. All infected neurons from sections including the frontal cortex through the dorsal hippocampus were then counted by region on the microscope. Representative confocal images of the somatosensory cortex, thalamus, and starter neurons were taken using an Olympus IX81 confocal microscope with the Fluoview FV1000 software.

Results of rabies tracing experiments were quantified by region as the percentage of inputs from that region over the total inputs received by the starter population. For the quantification of Layer I (LI) inputs to *Emx1* cells, the percentage of total cortical inputs (excitatory neurons and interneurons) over total inputs, or of the percentage of cortical interneurons alone over total inputs were quantified (Figure 7B). We were able to target a small population of starter cells (2–253 starter cells; Figure S6A) due to the focality of the rabies injection combined with very sparse electroporation of interneurons, which was further diluted by their dispersion during tangential migration to the cortex. The identities of starter cells and their presynaptic partners were confirmed by analyses of morphological features and laminar location (Figure 3B). The numbers of starter cells were not significantly different between P6 and P12 (Figures S6A and S6B), and were not correlated with the percentage of thalamic inputs received (Figure S6C). The number of presynaptic connections received by different cell types (5HT3aR Re, VIP, PC), however, were significantly different and, therefore, the comparison between cell types was done with regards to their respective percentage of thalamic inputs (Figure S6J). To assess whether the variability in the number of starter cells between the first and the second postnatal weeks could explain differences in thalamic contribution, we calculated the correlation between starter cell number and the proportion of thalamic inputs for each

week. We found that the percentage of thalamic inputs was not significantly correlated to the number of starter cells (FPW: $R^2 = 0.01$; SPW: $R^2 = 0.002$. [Figure S6C](#)). The functional status of these synapses was assessed by stimulating thalamic afferents optogenetically or electrically using slice electrophysiology ([Figures S6D–S6H](#)).

Immunohistochemistry

Immunohistochemistry on brain slices was performed as previously described ([De Marco García et al., 2011](#)). Electroporated neurons were identified by expression of eGFP (1:1000, Goat Anti-GFP, VRW). Identity of presynaptic partners illuminated by rabies tracing was determined by co-expression of mCherry (1:2000, chicken anti-RFP, VRW). In addition, immunohistochemistry against interneuron markers including reelin (1:500, mouse anti-reelin, VWR) and VIP (1:500, rabbit anti-VIP, Immunostar) was used to determine the identity of starter cells. GCaMP6s expression was evaluated using goat anti-eGFP (1:1000). Guinea pig anti-VGluT2 (1:1000, EMD Millipore) and Rabbit anti-SERT (1:10000, Immunostar) were used in barrel field analysis. Neurons filled with biocytin during whole-cell patch clamp recordings were labeled post hoc with streptavidin (1:1000, Streptavidin Pacific Blue, Thermo Fisher) and anti-reelin (1:1000). Neurons were imaged at 60X with an oil immersion objective (NA 1.4) at 0.5–1 μ m steps and traced using NeuroLucida 360 (2.70.5, 64 bit, MBF Bioscience). Morphological analysis was carried out on NeuroExplorer (Nex Technologies) as previously described ([De Marco García et al., 2011](#); [De Marco García and Fishell, 2014](#)). Images in [Figures 1A, 3D, 3H, 7A, 8A, 8D, 8E, S2A, S3A, S3F, and S7A](#) are composite images.

Barrel Field Analysis

5HT3aR.NR1^{fl/fl} and *NR1^{fl/fl}* littermates were perfused at P8, and brains were hemisected after post-fixation in 4% paraformaldehyde overnight. Hemispheres were flattened between two glass slides with glass spacers, fixed again overnight, then processed for sectioning and immunohistochemistry. All 36 posteromedial barrel subfield (PMBSF) principal barrels (A1–5, B1–4, C1–7, D1–8, E1–8, α - δ) were identified across sections ([Woolsey and Wann, 1976](#)). Sections in which barrels A1–4, B1–4, C1–5, D1–5, and E1–5 were identifiable and complete were chosen for barrel field morphology analysis ([Miceli et al., 2013](#)). The PMBSF and individual barrel areas were outlined manually with Fiji (ImageJ) software, and corresponding areas were measured. The summed areas of individual barrels were used for measurement of total barrel area and summed areas of individual barrels in rows A–E were used for row surface area measurements. DAPI was used to quantify cell density.

For septal width and barrel/septa boundary analyses, a custom written MATLAB (Mathworks) program was used to generate average fluorescence intensity curves for a row D. A 45-pixel width box spanning barrel centers and inter-barrel septa was drawn along the row, average fluorescence intensity was calculated along the length of the box, and an intensity curve was generated. A straight line was drawn to demarcate the septal wall. The slope (intensity units/distance) was calculated and used as a measure of axonal density in the barrel/septa boundary ([Figure 8G](#)). Slopes were measured on both sides of a given septa (D row) and averaged together ([Miceli et al., 2013](#)). Septa width was calculated as the distance across the intensity nadir. The MATLAB program used for these analyses is available upon request.

Cranial Window Surgery

Mice aged between P5–P6 were briefly anesthetized by ice-induced hypothermia for 5 min and then placed on a Snuggle Safe warmer (Lenric C21) for the remainder of the surgery. The surgical procedures were similar to previously described methods ([Rajasekharan et al., 2015](#)). The head was scrubbed with alternating solutions of 70% ethanol and 10% povidone-iodine (Betadine). All surgical surfaces and instruments used were sterilized. Local anesthesia was provided by infiltrating bupivacaine (Marcaine 0.25%–0.5% solution) into the tissue adjacent to the intended incision lines. Scalp above the somatosensory cortex determined by stereotaxic coordinates (centered at [from Lambda]: AP 1.6–2.2, ML 1.8–2.0, DV 0.1–0.3) was removed, a custom-made, titanium head plate for small mouse pups was positioned over the area, centered around the location marked for S1 with empirically tested coordinates adjusted for the age of pups, and finally, was adhered to the skull using a veterinary adhesive (Metabond). After the head plate implantation, the mouse was placed back on ice for 2–3 min if tail-pinch reflex had returned. A craniotomy (2–4 mm in diameter) was performed at the center of the circular head plate by gently etching away the skull using the sharp edge of a sterile 16G or 18G syringe needle. After achieving haemostasis, a cranial window (3 mm round #0, 0.1 mm, Warner instruments) was lowered on top of the brain, and warm (37°C) 1% agarose was applied to the perimeter of the craniotomy to seal it. The window was then fixed to the skull using veterinary adhesives (first Vetbond, then Metabond). The pup was then placed on a heating pad with bedding for recovery.

In Vivo Two-Photon Calcium Imaging

Mouse pups were allowed to recover on a heating pad for a minimum of 1 hr after surgery was completed. Recordings were performed on unanaesthetized mouse pups in which the head was stabilized by attaching the head plate to a fixed fork positioned beneath the objective using two set screws. The pup was kept on a 37°C heating pad and cotton balls or bedding were placed loosely around the animal for comfort. During imaging sessions, mouse pups spent the majority of time in a quiet resting state, interrupted by occasional limb or tail twitches.

A FluoView FVMPE-RS multiphoton imaging system (Olympus) was used for detecting brain activity in mouse pups. A Mai Tai Deepsee Ti:Sapphire laser (Spectra-physics) was tuned to 920 nm for GCaMP6s excitation and the total laser power delivered to the brain was less than 60 mW. A 25X (1.05 NA) water immersion lens (Olympus) was used for imaging. To ensure that LI was

consistently imaged in *5HT3aR.Cre*, *GCaMP6s*; *Wnt3a^{Cre}*, *GCaMP6s*; and *Sert^{Cre}*, *GCaMP6s* mice, we performed recordings at 40–60 μm below pia surface. Due to the absence of *Emx1*, *Lhx6*, and largely VIP somata in LI, *VIP.GCaMP6s*, *Lhx6.GCaMP6s*, *Emx1.GCaMP6s* mice and *GCaMP6s* driven by viral expression were imaged between 100–200 μm below pia surface, unless otherwise specified. Despite the position of their somata, all these populations project dendrites to LI (Lee et al., 2013; Staiger et al., 2015; Muñoz et al., 2017) and therefore have the potential to sample the same information as LI 5HT3aR interneurons. Despite the presence of a small number of Re-negative, non-VIP, 5HT3aR interneurons in our functional analyses (Figure S2C), 5HT3aR interneurons exhibit coherent activity patterns in layer I (Figure 1), pointing to a similar function at early developmental stages. Further cell-type-specific differences are likely to arise later in development (Tremblay et al., 2016). Image frames of 509 \times 509 μm (512 \times 512 pixels) were recorded using a Galvano scanner at a rate of 1 Hz. The large field of view (FOV) was used in order to capture as many interneurons as possible in a recording (one FOV typically contains 40–80 *5HT3aR.GCaMP6s* neurons). For a subset of experiments, we also imaged using a resonance scanner at 5 Hz (66 ms per frame, averaged every three frames) to achieve faster frame rate. Results using different scanning rates were comparable due to the slow kinetics of developmental calcium transients and of *GCaMP6s*. The laminar boundary between LI and LII was first determined by imaging *Emx1.GCaMP6s* mice and locating the depth at which pyramidal neurons first appeared. Each recording consisted of a single, continuous 9-min movie. Movies taken from non-overlapping FOVs were used for analysis. The system was controlled by FV30S-SW software (Olympus).

For chronic imaging, mice were returned to their home cage with the dam at the end of the initial imaging session on the day of the surgery or were imaged starting from the day after the implantation. The condition of the animal, head plate, and cranial windows were monitored daily. Subsequent imaging sessions took place every 24 hr, until the animal was sacrificed (typically between P12–P15). During each imaging session, the same FOV was located using blood vessels and the borders of the cranial window as landmarks. Imaging depths were adjusted as the animal matured to ensure that the same cohort of neurons was imaged. In some cases, the same neurons could be tracked daily during the entire span of the experiment (about 1 week, Figure S1). The presence of the head plate did not appear to impair feeding, grooming, or interactions between the pup and its mother as well as littermates. By the time they were sacrificed, body size in head-implanted animals did not differ from that of their littermates, nor did these animals display any gross developmental impairment. A cohort of pups was allowed to survive until well into adulthood, and no long-term impact of chronic head plate implantation was observed in this cohort (Figure S1).

After the last imaging session, the mice were sacrificed and the location of the cranial window was confirmed by topically placing Dextran (ThermoFisher) or DAPI (1:1000, ThermoFisher) over the window after removing the circular glass. Immunohistochemistry was also performed for anti-eGFP to check for expression of *GCaMP6s* (Figure 1A). The density of *GCaMP6s*-expressing neurons captured in post hoc staining was comparable to numbers observed in *in vivo* imaging (Figure S2). Since excitatory Cajal-Retzius (CR) cells also express 5HT3aR (Inta et al., 2008; Lee et al., 2010), we excluded from our analysis small neurons with elongated somata ($10.9\% \pm 3.9\%$ of 5HT3aR neurons), a morphology typical of these cells (Schwartz et al., 1998; Chowdhury et al., 2010), and only scored calcium transients in interneurons characterized by large somata (Figure S2H). In addition, we determined CR cell activity by targeting *GCaMP6s* expression to this population with a *Wnt3a^{Cre}* driver line (Figures S2J–S2L). CR cells identified both morphologically and genetically showed very few calcium transients at P6 (Figures S2I, S2K, and S2L).

We did not observe any developmental or behavioral abnormalities in any of our *RCL-GCaMP6s* (*Ai96*) mice, or mice expressing *GCaMP6s* from our *Cre* line crosses. In particular, we did not observe any pathology in *Emx1Cre.Ai96* mice used for this study or in our current large colony ($n = 70$ mice \times ~ 10 generations, 700+ mice) in agreement with a recent report indicating that epileptiform activity was not observed in *Emx1Cre.Ai96* mice (Steinmetz et al., 2017). Furthermore, in support for a lack of cellular pathology, *GCaMP6s*-expressing cells show no signs of toxicity or developmental defects. Cell migration and survival, as well as intrinsic electrophysiological properties of *GCaMP6s*-expressing neurons were not significantly different from those of controls (Figure S3; Tables S1 and S2). In particular, nuclear inclusions, which are frequently associated with cytotoxicity, were not observed in these cells at the stages analyzed (Figures S3C and S3D). Finally, we have compared spontaneous calcium activity in pyramidal cell populations that either expressed *GCaMP6s* from the *Ai96* transgene since the progenitor stage (*Emx1Cre.GCaMP6s*) (Stirman et al., 2016) or after AAV viral infection starting at P0 (AAV.Syn*GCaMP6s*) (He et al., 2017). Our P6 *in vivo* recordings revealed no significant differences in event frequency or correlation (Figures S3I–S3L). In addition, the sensor was able to detect single action potentials (APs), and spontaneous events recorded electrophysiologically show perfect correspondence with calcium transients, consistent with previous reports in the adult brain (Chen et al., 2013) (Figure S4). Altogether, these observations indicate that *GCaMP6s* expression does not cause pathological phenotypes.

Whisker Stimulation

Whisker stimulation was performed by air puff given through a 1 mm diameter tube placed anterior and perpendicular to the whiskers, approximately 1 cm away. Stimulation was directed to the snout. Each air puff was about 100 ms, gated by a solenoid valve controlled by a TTL signal from the imaging FV30S-SW software via an Arduino board (Arduino Diecimila). The pressure of the air puff was adjusted so that all whiskers on the whisker pad were displaced, but the mouse was not startled and did not display any signs of discomfort. The TTL signal was triggered at the onset of the frame scan every 50 frames for recordings with a 1 Hz frame rate, or every 250 frames for recordings with a 5 Hz frame rate. This strategy allowed for inter-stimulus intervals of approximately 50 s to allow sufficient baseline recordings after each stimulation.

Imaging Data Processing and Transient Detection

Image processing and calcium-signal detection were carried out using CalciumDX software routines written in MATLAB (Mathworks) (Ackman et al., 2012), available open source in GitHub repository (<https://github.com/ackman678/CalciumDX>). Movies were first motion corrected to account for small xy displacement using the Image Stabilizer plugin for NIH ImageJ, which uses the Lucas-Kanade algorithm to estimate the geometrical transformation needed to best align each frame to a reference frame (http://www.cs.cmu.edu/~kangli/code/Image_Stabilizer.html). To ensure imaging data were collected from un-anaesthetized neonatal mice that are quietly resting with only cardiopulmonary or myoclonic twitch movements, recordings containing segments of large motion artifacts were excluded from the analysis. For each movie, cell contours were semi-automatically detected in the *t*-stack projections of the average intensity image using an edge-detection algorithm, and calcium signals were measured as the average intensity inside each cell contour (Allène et al., 2008; Crépel et al., 2007; Ackman et al., 2012). Activity patterns in thalamic axonal arbors as labeled in *SERT*. GCaMP6s mice were analyzed as regions of interest (ROIs) by applying a grid over the images obtained from calcium recordings (Ackman et al., 2012; Peron et al., 2015). The $\Delta F/F$ signal was then calculated for every contour/grid in each frame. Calcium transients were identified using automatic detection algorithms. Briefly, baseline de-trending was performed by applying a high pass filter, and a temporal sliding window with a length of 3 frames was used to determine baseline average (Dombeck et al., 2007). The threshold of detection was set as 2 standard deviations above the baseline average plus 2 standard deviations above the derivative of the signal (local maxima). The onset of calcium events was set as the first frame in the rising phase of the calcium transient, and the offset was set as the half-amplitude of the decay time. Active cells are neurons with at least one detected calcium event during the entire movie. Neuropil signals were measured for neuropil correction in a subset of neurons ($n = 10$ movies) by drawing a shell around the detected soma. The radius of the shell was calculated by keeping the area of the shell (the area between the neuropil outline and the soma outline) to be the same as the soma area. The corrected signal was determined by subtracting the neuropil signal measured in the shell from the soma signal. This was performed on P6 and P12 5HT3aR Re interneurons and P6 VIP interneurons. The differences between frequency and correlation comparisons still held after correction.

In this study, we aimed to assess the influence of activity patterns in the establishment of circuit formation. Calcium imaging analyses in developing neurons are frequently used to compare network activities of neuronal populations at different developmental stages (Allène et al., 2008; Golshani et al., 2009; Burbidge et al., 2014). In sensory cortices, spontaneous APs appear in bursts and may be required for efficient activity-dependent transcription and synapse stabilization during development (Garaschuk et al., 2000; Rochefort et al., 2009; Egorov and Draguhn, 2013). Indeed, due to the prominence of NR2B-containing NMDAR receptors and the longer duration of EPSCs in development, temporal summation and large amplitude calcium events are frequently generated in response to spontaneous activity containing bursts of APs (for review, see Moody and Bosma, 2005). Based on its high sensitivity and slow kinetics, GCaMP6s is well suited to detect this type of calcium event. Although burst firing is prominent in development, it is formally possible that some neurons would fire isolated spikes. If GCaMP6s fails to detect single APs, these events would be missed and could artificially increase the degree of synchrony in our analyses. To address this possibility, we performed simultaneous patch clamp recordings and calcium imaging. In agreement with previous observations (Allène et al., 2008), we found that spontaneous activity in interneurons and pyramidal cells largely consists of AP bursts with long intervals of silence at P6 and P12 (Figure S4). In addition, single APs invariably produced calcium events, indicating that AP underestimation due to detectability differences among cell types or developmental stages is unlikely (Figures S4A and S4B). Since calcium events were always associated with APs in our observations, it is also unlikely that our analysis represents an overestimation of neuronal activity (Figure S4). Since we used event onset to quantify cell pairs with correlated activity and all spikes we observed are detected by GCaMP6s, and given that the purpose of our current study is not to decode firing rate or precise timing, any nonlinearity of transfer functions, if existent, would not affect our results. In addition, the linearity of the transfer functions for GCaMPs in adults has been shown in selected subtypes, and its sensitivity and consistency are well-recognized in many recent studies using GCaMP calcium imaging in different subtypes of adult interneurons (Kwan and Dan, 2012; Chen et al., 2013; Pinto and Dan, 2015; Karnani et al., 2016; Batista-Brito et al., 2017).

Imaging Data Analysis

Data were analyzed using custom routines written in MATLAB as previously described (Allène et al., 2008). To characterize calcium activity patterns for individual neurons, we quantified calcium transient frequency, which was measured both as inter-event interval (s) and number of events per second (mHz) for each cell as well as duration, which was measured as the time between onset and offset of a calcium event. The frequency and duration were measured for each cell (or ROI), then averaged over all the cells in one movie. To identify significant correlation between any two cells within a recording, the onset of each event was represented by a Gaussian (± 1 frame), and distance correlation values were calculated. Given the prolonged silent periods we observed typical in developing neuronal networks (inter-event interval of 24 – 500 s), we think this method is an appropriate method for quantifying synchronous calcium activity at this stage. The significance of the correlation was determined via permutation testing by comparing the correlation value to a distribution of correlation values from 1000 randomized datasets where events were reshuffled. We used a threshold significance level $p < 0.01$ for stringency. Percentage of cell pairs that were significantly correlated was reported for each recording. In some cases, for demonstration purposes, Pearson's correlation coefficients were also reported. Synchronicity of network activity was quantified as previously described (Allène et al., 2008; Golshani et al., 2009; Schwartz et al., 1998). Event histograms that plotted the percentage of cells active for each frame were first constructed. In order to determine the percentage of cells that must be simultaneously active to represent a statistically significant network event, surrogate activity histograms

were constructed by reshuffling events in each cell, and were repeated 1000 times to create a distribution of event sizes. The threshold significance for network events was then set at $p < 0.01$. The time points where the percentage of cells active exceeded or dropped under the threshold were set to be respectively the onset and offset of network events. These time points were used to quantify the duration of network events. The magnitude of network events was quantified as the peak percentage of cells coactive in each network event and was averaged for all events across a movie. For movies recorded during whisker stimulation, network events were first identified as described above, and events with peak time within 5 s after the trigger of air puff were deemed as evoked by stimulation. The number and magnitude of evoked network events was quantified for each movie.

Statistical analyses were performed on the mean of all movies from multiple animals for each genotype, treatment group, and developmental stage. If more than one movie from the same mouse were used for a given age, these movies corresponded to non-overlapping FOVs and therefore consisted of different cell populations. We used either unpaired Student's *t* tests (or Mann-Whitney test) or ANOVA followed by Bonferroni multiple comparisons test (or Kruskal-Wallis test followed by Dunn's multiple comparisons test), as indicated in the Results section and figure legends. The sample sizes used were comparable to previous publications (Ackman et al., 2012; Kirmse et al., 2015; Kamani et al., 2016).

Sensory Deprivation

Sensory deprivation by whisker plucking was performed as previously described (De Marco García et al., 2015). In brief, newborn pups were subjected to whisker plucking daily from P0 to P6 or P12. Pups from the same litter were randomly divided into deprived and control groups. Pups from both groups were briefly removed from the dam and anesthetized by hypothermia (3–5 min) before P6, or by isoflurane after P6. In the sensory deprived group, all whiskers and most of the facial hair on the whisker pads were plucked bilaterally using sterile forceps, whereas in the control group whiskers were spared (see also De Marco García et al., 2015). Subsequently pups were allowed to recover on a heating pad before returning them to their dam.

Electrophysiology

Whole-cell patch-clamp recordings were performed on 5HT3aR Re neurons within layer I in acute brain slices. Neuronal identity was confirmed by post hoc morphological analysis and by immunohistochemistry against Reelin in filled cells. P5–P6 mice were used for recordings of NMDA/AMPA ratio, while P6–P8 and P12–P15 mice were used in experiments recording thalamocortical responses in 5HT3aR Re interneurons. Mice were deeply anaesthetized on ice (if P6 or younger) or by isoflurane (if P7 or older) and then decapitated. Brains were rapidly removed and immersed in ice-cold oxygenated (95% O₂ and 5% CO₂) dissection buffer containing (in mM): 83 NaCl, 2.5 KCl, 1 NaH₂PO₄, 26.2 NaHCO₃, 22 glucose, 72 sucrose, 0.5 CaCl₂, and 3.3 MgCl₂. Coronal slices (300 μ m) were cut using a vibratome (VT1200S, Leica) and incubated in dissection buffer for 40 min at 34°C. Slices were stored at room temperature for remainder of the recording day. All slice recordings were performed at 34°C unless otherwise specified. Slices were visualized using IR differential interference microscopy (DIC) (BX51WI, Olympus) and a CMOS camera (ORCA-Flash4.0 LT, Hamamatsu). Regions of interest on the slice (i.e., barrel cortex, VPM) were visualized and identified using a 10X Olympus objective (0.3 NA), and individual cells were visualized with a 60x Olympus water immersion (1.0 NA) objective.

For all recordings, external buffer was oxygenated (95% O₂ and 5% CO₂) and contained (in mM): 125 NaCl, 25 NaHCO₃, 1.25 NaH₂PO₄, 3 KCl, 25 dextrose, 1 MgCl₂, and 2 CaCl₂. Patch pipettes were fabricated from borosilicate glass (OD 1.5/ID 0.86, Sutter Instrument) to a measured tip resistance of 3–6 M Ω . Signals were amplified with a Multiclamp 700A amplifier (Molecular Devices), digitized with an ITC-18 digitizer (HEKA Instruments) and filtered at 2 KHz. Data were monitored, acquired and, in some cases, analyzed using Axograph X software. Series resistance was monitored throughout the experiments by applying a small test voltage step and measuring the capacitive current. Series resistance was 5–25 M Ω and only cells with < 20% change in series resistance and holding current were included for analysis. Liquid junction potential was not corrected.

For experiments measuring NMDA/AMPA ratio, recordings were performed on LI neurons that expressed Re, confirmed by post hoc immunohistochemistry. Pipettes were filled with an internal solution containing (in mM): 110 CsMeSO₄, 10 CsCl, 10 HEPES, 10 Cs₄-BAPTA, 5 QX-314•Br, 0.1 spermine, 4 Mg-ATP, 0.4 Na-ATP, 10 phosphocreatine, 0.05% biocytin, adjusted to pH 7.3 with CsOH and to 278 mOsm with double-distilled H₂O. Recordings began at least 10 min after initial whole-cell patch was achieved to allow dialysis of Cs⁺ internal solution. EPSCs were evoked using an isolated pulse stimulator unit (ISO-Flex, A.M.P.I.) with a tungsten bipolar stimulator (Harvard apparatus), placed 150–200 μ m ventro-laterally to the recording pipette. A single extracellular stimulation was delivered every 15 s, and 30–50 responses were averaged. All recordings were performed in the presence of the GABA_A receptor blocker SR-95531 (Gabazine, 5 μ M, Abcam Biochemicals). AMPAR-mediated currents were recorded at –70 mV, whereas NMDAR-mediated currents were recorded at +40 mV in the presence of NBQX (10 μ M).

For experiments measuring thalamocortical responses using optogenetic or electric stimulation, pipettes were filled with an internal solution containing (in mM): 125 CsMeSO₄, 10 TEA Cl, 10 HEPES, 0.1 EGTA, 4 Mg-ATP, 0.3 Na-ATP, 10 phosphocreatine, 0.05% biocytin, adjusted to pH 7.3 with CsOH and to 278 mOsm with double-distilled H₂O. Thalamocortical slices were prepared following methods described previously (Agmon and Connors, 1991; Porter et al., 2001). For electric stimulation, the stimulating electrode was placed in the VPM or the border of VPM and internal capsule, while recordings were made in LI 5HT3aR Re interneurons. For optogenetic stimulation experiments, TTX (1 μ M) and 4-aminopyridine (1.2 mM) were present in the bath (De Marco García et al., 2015). The Blue light source (470 nm, Polygon 400) was mounted on the microscope between the camera and the objective, reaching the slice by means of a dichroic mirror through the 60X objective. The intensity was set to 100% and the duration was adjusted to obtain

optimal monosynaptic responses (0.2–2 ms long). For stimulation of LI only, the stimulation region was drawn on the FOV with the patched cell in the center, limited to LI, with the Polygon 400 software.

For experiments evaluating the sensitivity and reliability of GCaMP6s, *5HT3aR.GCaMP6s* mice between P6 – P12 and *Emx1.GCaMP6s* between P6 – P7 were used for slices. Horizontal sections were cut in order to promote spontaneous activity (Allène et al., 2008). Regions and cells with detectable spontaneous activity were first identified with the 4X and 60X objective. Once whole-cell patch clamp was achieved on the cell of interest (usually with low or no visible baseline fluorescence), 180 s current-clamp charts were recorded while wide-field images were captured simultaneously using a CMOS camera (ORCA-Flash4.0 LT, Hamamatsu). Movies were analyzed using the same method as 2-photon imaging.

For current clamp experiments, pipettes were filled with an internal solution containing (in mM): 125 potassium gluconate, 10 KCl, 10 HEPES, 4 Mg-ATP, 0.3 Na-GTP, 0.1 EGTA, 10 phosphocreatine, 0.05% biocytin, adjusted to pH 7.3 with KOH and to 278 mOsm with double-distilled H₂O. Data analysis was performed using Axograph X built-in analysis and IGOR Pro software (Wavemetrics) on a Macintosh computer.

Tactile Discrimination Task

Fourteen male control *NR1^{fl/fl}* and 8 male *5HT3aR.Cre, NR1^{fl/fl}* mutant mice were tested on an adapted tactile discrimination task (Wu et al., 2013), based on the general principles of a novel object recognition task (using vibrissal rather than visual input). The test apparatus was a (30 cm × 30 cm × 18 cm) plexiglass arena with opaque walls. The target “objects” were 5 cm × 9 cm sheets of aluminum oxide sandpaper (3M, St. Paul, MN) affixed to the lateral walls of the test chamber (right and left sides), at the bottom of the far back corner. Two different grades of sandpaper were used for the texture discrimination task; 80- and 180-grit (average particle width of 190 μm and 82 μm, respectively).

For the tactile discrimination task, the following experimental protocol was used (Figure 8): One day prior to testing, subjects were habituated to the testing chamber for 10 min. On testing day, subjects were given one additional habituation period for 5 min, immediately followed by a 5-min “familiarization” period where they were exposed to two identical sheets of either 80- or 180-grit sandpaper (this “familiar” grit was randomized so that half of each group experienced 80-grit as the familiar texture while the other half experienced 180-grit as familiar), each located opposite from one another on the lateral walls. During the familiarization phase, subjects were placed in the center of the testing chamber, equidistant and facing away from the identical textured sandpaper. Following the familiarization phase, subjects were returned to their home cage for a 5-min resting period. During the resting period, the textured sheets used during the familiarization phase were removed and replaced with one identical “familiar” sheet and one “novel” sheet of the alternative grit. The side with the novel texture was chosen for each animal as the less preferred side during the familiarization period. Following the resting period, subjects were placed back into the testing chamber for a final 3-min testing period. Behavioral video tracking and quantification was performed using Ethovision XT (Noldus Information Technology) to automatically determine when subjects were investigating the sandpaper objects. Interaction was considered any time in which the subject’s nose point entered a 3 cm × 9 cm zone in front of the sandpaper on either side of the chamber.

QUANTIFICATION AND STATISTICAL ANALYSIS

Statistics were performed using Prism 7 software (Graphpad), and graphs were generated in Prism 7, IGOR Pro software, or MATLAB. For analyses on imaging experiments, *n* refers to the number of movies unless otherwise specified; for immunohistochemistry and rabies tracing experiments, *n* refers to the number of mice; for electrophysiological experiments, *n* refers to the number of neurons recorded. The *n* for each experiment was indicated once in the figure legend in the first quantification panel for the particular comparison. Frequency (Figure 1E) and duration (Figure 1F) data from P6 5HT3aR Re videos are also shown in Figures 2C, 2D, and 4E to facilitate comparison with P12 and thalamic events. Normality tests were first performed to determine if datasets were normally distributed. For datasets that follow normal distribution, statistical significance was determined using either Student’s *t* tests (indicated on graphs with asterisks, **p* < 0.05; ***p* < 0.01; ****p* < 0.001, *****p* < 0.0001; ns, *p* > 0.05) or ANOVA (indicated by *p* values in legends as well as results). For multiple comparisons tests following ANOVA, multiplicity adjusted *p* values were reported (indicated on graphs with asterisks, **p* < 0.05; ***p* < 0.01, ****p* < 0.001, *****p* < 0.0001; ns, *p* > 0.05). For data involving proportions as dependent variables, the arcsine-square-root transformation was first performed before ANOVA analysis. For datasets that did not have normal distributions or were too small to merit a normality test, Mann-Whitney test or Kruskal-Wallis test followed by Dunn’s multiple comparisons test were used. Significance was based on *p* values < 0.05. Means and standard errors were reported for all results unless otherwise specified.